Acta Mech 233, 2615–2651 (2022)
https://doi.org/10.1007/s00707-022-03239-x

ORIGINAL PAPER

Uri Breiman · Ido Meshi · Jacob Aboudi · Rami Haj-Ali

Finite strain PHFGMC micromechanics with damage and failure

Received: 21 October 2021 / Revised: 6 March 2022 / Accepted: 11 April 2022 / Published online: 17 June 2022

Abstract The parametric high-fidelity generalized method of cells (PHFGMC) is further developed for the prediction of damage and progressive failure of composites undergoing large deformation. The mechanical behavior of the constituents is described using hyperelastic strain energy functions with embedded energy limiters in order to bound the amount of accumulated energy during deformation. The proposed nonlinear micromechanical theory generates both the local and overall global responses, including the effective instantaneous stiffness tensor of the composite. To solve the PHFGMC equations, i.e., equilibrium, continuity and periodicity, and constitutive relations, an incremental-iterative scheme is offered in this study. The iterative scheme is needed in order to develop a progressive failure methodology which enables the determination of the current stress distribution during the applied loading. Applications are given for several case studies demonstrating the effects of the mechanical properties of the constituents (elastic anisotropy and failure parameters), and the geometrical features of the composite (fiber–matrix interphase and fiber waviness), on its overall stiffness and strength. Experimental testing and results from this study and the literature are used for the calibration of the constitutive material properties. This calibration is extensively elaborated and performed to generate the PHFGMC multi-axial effective strength envelopes of the calibrated IM7/977-3 carbon/epoxy composite.

List of symbols

Continuum mechanics

$\mathbf{F}$	Deformation gradient tensor
$\mathbf{C}$	Right Cauchy–Green deformation tensor
$\mathbf{E}$	Green–Lagrangian strain tensor
W	Strain energy function
I_1, I_2, I_3	First, second, and third invariants of $\mathbf{C}$
I_4, I_5	Fourth and fifth pseudo-invariants of $\mathbf{C}$
$I_1^{'}, I_2^{'}$	Reduced first and second invariants of $\mathbf{C}$

R. Haj-Ali (✉)
School of Mechanical Engineering, Tel Aviv University, Haim Lebanon, Tel-Aviv 6997801, Israel
E-mail: rami98@tauex.tau.ac.il

U. Breiman
E-mail: uribreiman@mail.tau.ac.il

I. Meshi
E-mail: idomeshi@mail.tau.ac.il

J. Aboudi
E-mail: aboudi@eng.tau.ac.il

$\mathbf{A}, \theta$	Axis of symmetry direction vector and angle
$\mathbf{P}, \mathbf{S}$	First and second Piola–Kirchhoff stress tensors
$\mathbf{R}, \mathbf{D}$	Instantaneous tangent stiffness tensors
δ_{ij}	Kronecker delta

Mechanical properties

λ, μ	Lamé constants
φ, ζ, η	Transversely isotropic material parameters
E_L, E_T	Longitudinal and transverse Young's moduli
ν_L, ν_T	Longitudinal and transverse Poisson's ratios
G_L	Longitudinal shear modulus
κ	Bulk modulus
$\mathrm{C}_{10}, \mathrm{C}_{01}$	Hyperelastic coefficients
$(\cdot)^{\check{f}}$	Fiber phase value
$(\cdot)^{\check{m}}$	Matrix phase value
$(\cdot)^{\check{i}}$	Interphase value

Damage and failure modeling

ψ, ψ^F, ψ^E	Modified, failure, and elastic strain energy functions
ϕ, ϕ_C	Limit and critical energies
m	Energy-drop sharpness
Γ	Upper incomplete gamma function
ψ_{C_L}, ψ_{C_H}	Low and high critical energies
ϵ	Failure stiffness coefficient

PHFGMC micromechanics

$\mathbf{X}, \mathbf{Y}$	Physical macroscale and microscale coordinates
$\mathbf{r}$	Parametric microscale coordinates
$H_1, .., H_4$	Bilinear mapping shape functions
$\mathbf{Y}^{(1)}, .., \mathbf{Y}^{(4)}$	Location of the subcell's vertices
$\mathbf{u}$	Displacement vector
$\mathbf{w}_0, .., \mathbf{w}_4$	Microvariables
$\check{\mathbf{J}}$	Jacobian matrix of the inverse mapping
$\mathbf{A}_{\mathrm{W}}$	Deformation gradient–microvariables coefficient matrix
β_k	Edge k of subcell β
$\Pi, \Pi_{\mathrm{int}}, \Pi_{\mathrm{ext}}$	Total, internal, and external (work) energies
$\mathbf{I}^0_{\mathrm{F}}, \mathbf{I}_{\mathrm{W}}$	Internal macro- and micro-resisting vectors
$\mathbf{Q}^0_{\mathrm{F}}, \mathbf{Q}_{\mathrm{W}}$	External macro- and micro-resisting vectors
$\mathbf{R}^{es}_{\mathrm{F}^0}, \mathbf{R}^{es}_{\mathrm{W}}$	Overall macro- and micro-residual vectors
$V^{(\beta)}, V_{RUC}$	Volume (area) of subcell β and of the repeating unit cell
$\mathbf{K}_{\mathrm{WW}}, ..., \mathbf{K}_{\mathrm{F}^0\mathrm{F}^0}$	The four partitions of the 'stiffness matrix'
$\mathbf{G}$	Concentration tensor
N_{SC}	Total number of subcells in the repeating unit cell
$\bar{(\cdot)}$	Average value
$\tilde{(\cdot)}$	Fluctuation value
$(\cdot)^{(\beta)}$	Subcell β's value
$(\cdot)^0$	Remote (macroscale) value
$(\cdot)^*$	Effective (macroscale) value
$\hat{(\cdot)}$	Trail iterative value
$(\cdot)^{(q,n)}$	Value of the argument at increment q, iteration n

Composite's geometrical dimensions

H, L	Overall height and thickness of the model
v_f, d_f	Fiber volume fraction and diameter
d_m	Total matrix thickness
x_f, x_m	Thickness of individual fiber and matrix subcells
u_2^0, u_2^I	General waviness function and amplitude
u_{2f}^I, u_{2m}^I	Specific waviness function at the fiber and matrix regions

Other symbols

$\mathrm{tr}(\cdot)$	Trace operator
$\det(\cdot)$	Determinant operator
$(\cdot)^{\mathrm{T}}$	Transpose operator
$(\cdot)^{-1}$	Inverse operator
$(\cdot) \cdot (\cdot)$	Dot product
$(\cdot) : (\cdot)$	Double dot product
$\Delta(\cdot)$	Incremental value
$\exp(\cdot)$	Exponent in the power of the argument
$sin(\cdot)$	Sin function of the argument
$\delta(\cdot)$	Variation of the argument
i, j, k, l	Indices for arrays, vectors, matrices, and tensors

1 Introduction

Due to their heterogeneous nature, composite materials and structures are susceptible to damage and failure during manufacturing and service. Extensive efforts for predicting the failure of fibrous composites were reported in the worldwide failure exercises [1–3], and more recently by Engelstad and Clay [4], for example. In these examples, several worldwide leading groups attempted to evaluate the mechanical response of laminated coupons and found it to be a challenging task to accurately predict the composite's strength for all load cases. To that end, computational and analytical tools were developed to capture the composites' mechanical response and strength for specific stress states. Thus, for example, Daum et al. [5] presented a review of such attempts for the compressive strength of laminates. In addition, the analysis of different composite systems requires the formulation of particular analytical and numerical governing equations. Thus, since standard epoxy-based composites have different microstructures than biological tissues, the damage and failure modeling will also differ between these two composite systems. See Orifici [6] and Li [7] for extensive examples of damage and failure modeling of standard composites and soft tissues, respectively.

One approach to analyze the composite is to adopt macroscale theories where closed-form analytical representations of the anisotropic stiffness tensor are assumed for the effective elastic behavior of the composite. For linearly elastic composites, damage is introduced as a weakening of the stiffness tensor components, see Voyiadjis and Kattan [8] and Aboudi et al. [9], for several examples. For composites undergoing large deformation, however, the effective response is modeled by anisotropic strain energy functions, and the effect of anisotropy is captured by incorporating at least five strain-invariants, see Jha et al. [10], Nolan et al. [11], and Gracia-Gonzales et al. [12] to name a few. Furthermore, it is necessary to assume specific functions in the strain energy and incorporate additional terms to account for characteristic features such as fiber orientation, distribution, and strength. This obviously complicates the choice of the proper constitutive energy function and the additional terms in order to calibrate the considered composite correctly. Such efforts were previously established for biological tissues as reviewed by Holzapfel et al. [13]. However, it is clear that by adopting this macro-approach, the computation time of the model will be quite short since it involves a direct use of anisotropic constitutive relations. This is in contradistinction to a micromechanical analysis, which is described in the following, where a large system of equations needs to be solved.

In a micromechanical approach, designated to analyze the composite's behavior, the microstructure of the heterogeneous material is explicitly considered. This is achieved by a micromechanical analysis in which the constitutive relations of the constituents and their detailed interactions are considered. For composites with

periodic microstructures, this methodology allows defining a representative volume element known in this case as a repeating unit cell (RUC). Furthermore, the commonly used isotropic constituents can now be modeled with isotropic energies that depend only on three invariants. This significantly reduces the complication of calibrating the macro-energy function of the entire composite to simply calibrating the isotropic energy of the phases. Once setting these values, it is possible to analyze other composites which are composed out of the same constituents but with different geometrical structures (e.g., fiber volume fraction, voids, microcracks, fiber waviness). In the previous macromechanical approach, on the other hand, any change of the microstructure requires a recalibration of the composite's macro-energy, which obviously forms a significant disadvantage, see [14–16], for example.

In the present study, the parametric high-fidelity generalized method of cells (PHFGMC) is employed to predict the finite strain mechanical response and strength of several composites. The PHFGMC is an extension of the high-fidelity generalized method of cells (HFGMC) that has been previously implemented for numerous mechanical problems, see Aboudi et al. [17] for extensive examples of micromechanical problems at infinitesimal and finite strains. Haj-Ali and Aboudi have presented the PHFGMC for doubly and triply periodic composites [18,19]. The main advantage of the PHFGMC is that it allows a better representation of fibers and inclusions, and partitioning of the RUC of the composite into an arbitrary arrangement of subcells, thus reducing the number of equations of the problem. Recent extensions of the PHFGMC at infinitesimal strains, which incorporate damage and failure effects in composites, were presented by Levi-Sasson et al. [20], Massarwa et al. [21,22], and Meshi et al. [23].

As to PHFGMC micromechanics at finite deformation, it was employed for the modeling of soft tissues by Breiman et al. [24]. Here, the nonlinear hyperelastic constitutive laws of Mooney–Rivlin and Yeoh were implemented to model the mechanical response of the collagen fibers and the elastin matrix of the composite. Results were presented for the response of the human abdominal aorta, which consists of three-layered tissues: intima, media, and adventitia. In this paper, however, damage and failure were not included in the formulation. Composite materials as those mentioned in [24] can be subjected to more significant deformations, leading to irreversible response until failure. For example, tissues can rupture under significant twists and movements during sports activities or accidents. Furthermore, the damage in composite materials that develops during service can initiate due to many reasons, and to form in a variety of damage mechanisms such as fiber tear, delamination in the structure, pullout of the fibers, to name a few. Therefore, the incorporation of damage and failure must be taken into account during the design process, where the damage modeling must describe the weakening and softening of the material during loading. In addition, the failure criterion will be used to limit the stress (or stretch) of the hyperelastic material (see Korenczuk et al. [25], Liu et al. [26], and Maiti et al. [27], for example).

There are several methods to model damage and failure of composites that undergo finite strain. In the work of Russ et al. [28], for example, the authors proposed constitutive damage laws for 3D-printed hyperelastic composites. They have presented a non-standard phase field fracture formulation to predict the progressive failure mechanism of a soft matrix reinforced with stiff circular inclusions. Their proposed damage model contained a strain energy density threshold that allowed to control the evolution of the fracture in the composite. In another research, Aboudi [29] presented micromechanically driven damage analyses for nylon-rubber-type composites at finite strains. Here, the Mullins damage phenomenon was modeled by employing the HFGMC micromechanics while using the constitutive damage formulation of de Souza Neto et al. [30].

An additional damage modeling method for finite strain, the energy limiters theory, was proposed by Volokh [31–33]. The objective of this model was to bound the amount of strain energy that can be accumulated during deformation. To that end, Volokh proposed modifying the energy function of the material such that, for a critical energy value, the material will not be able to store any more energy, even though it continues to deform.

The energy limiters theory was implemented within the HFGMC for several micromechanical problems by Aboudi and Volokh [34–36]. In [34], the response of a nylon-rubber composite in the presence of energy limiters was predicted. In addition, the effect on the response caused by the imperfect bonding between the phases was investigated. This enabled to generate initial failure envelopes for biaxial loading and the behavior of composite laminates. In [36], simulations of the HFGMC were performed for the prediction of the uniaxial stress–stretch response of soft tissues with (stiff) Calcium as the inclusion. These analyses were performed till initial failure using both doubly periodic and triply periodic composites for several inclusion volume fractions. In a more recent work of Aboudi and Volokh [35], the micromechanical modeling, that includes the energy limiters theory, was extended to account for the finite strain viscoelasticity of the phases.

All three papers mentioned above, [34–36], predicted the initial failure of the composites, implying that at any given failure at the microscale the analyses were terminated. One of the challenges in extending the analyses beyond initial failure is the occurrence of negative values of the tangent stiffness tensor of one or several subcells, thus leading to divergence of the incremental procedure. The progression of the failure, on the other hand, can indicate on specific failure mechanisms that occur afterward. For example, matrix cracking can lead to failure at the fiber–matrix interphase or to fiber breakage.

In the present investigation, an incremental-iterative numerical scheme for the solution of the finite strain PHFGMC equations, in conjunction with the incorporated energy limiters approach, is proposed for progressive failure. Here, the accumulated energies of the subcells during deformation are examined and compared with the critical energy values, in order to determine whether failure initiates in the subcells. In case of failure, the stiffness of the material within the subcell is reduced to a very small number, the stresses are transferred to their neighboring subcells, and the iterative procedure, which ensures that the tangent stiffness of all subcells remains positive, is continued. Furthermore, in the event of failure, the iterative scheme enables additional subcells to fail according to the new stress redistribution, thus progressing the failure in the composite.
In the present article, the finite strain PHFGMC is applied to several composites demonstrating progressive failure at a uniaxial stress state. In particular, the effects of geometrical dimensions of the composite, the anisotropy, and waviness of the constituents, as well as the axis of symmetry orientation, on the composite strength and behavior are examined. Additionally, the established PHFGMC micromechanics is employed to generate the failure envelopes of a commonly used composite system. Toward this goal, an extensive calibration scheme is described for the compressive and tensile characterization of the composite phases' energies.

This article is organized as follows. The constitutive formulations for isotropic and transversely isotropic materials with embedded softening and failure are given in Sect. 2. The micromechanical PHFGMC theory, formulated at finite strain, along with a newly proposed incremental-iterative numerical scheme, is presented in Sect. 3. Several applications are given in Sect. 4 demonstrating the PHFGMC capabilities to simulate and predict the overall macroscale response and the field distributions at the microscale. This includes the failure development of different composites at uniaxial and multiaxial load states. Conclusions and directions for future research are given in Sect. 5.

2 Finite strain materials with softening and failure

2.1 Finite strain constitutive and governing equations

Hyperelastic materials are represented by a strain energy function, W, which for isotropic materials is defined by the three invariants of the right Cauchy–Green deformation tensor, $\mathbf{C}$, namely $\mathrm{W} = \mathrm{W}(\mathrm{I}_1, \mathrm{I}_2, \mathrm{I}_3)$. These invariants are defined by (see [24])

$$\mathrm{I}_1 = \mathrm{tr}(\mathbf{C}), \quad \mathrm{I}_2 = \frac{1}{2}(\mathrm{tr}^2(\mathbf{C}) - \mathrm{tr}(\mathbf{C}^2)), \quad \mathrm{I}_3 = \det(\mathbf{C}), \tag{1}$$

and the right Cauchy–Green deformation tensor is defined by the deformation gradient tensor, $\mathbf{F}$, by $\mathbf{C} = \mathbf{F}^{\mathbf{T}} \cdot \mathbf{F}$. For a transversely isotropic material whose axis of symmetry is in the direction of vector $\mathbf{A}$, two additional pseudo-invariants are introduced as $\mathrm{I}_4 = \mathbf{A} \cdot \mathbf{C} \cdot \mathbf{A}$ and $\mathrm{I}_5 = \mathbf{A} \cdot \mathbf{C}^2 \cdot \mathbf{A}$, such that $\mathrm{W} = \mathrm{W}(\mathrm{I}_1, \mathrm{I}_2, \mathrm{I}_3, \mathrm{I}_4, \mathrm{I}_5)$.

Using the derivatives of the energy function with respect to the right Cauchy–Green deformation tensor, the second (symmetric) Piola–Kirchhoff stress tensor's components are given in Holzapfel [37] and defined as

$$S_{ij} = 2\frac{\partial \mathrm{W}}{\partial C_{ij}} \tag{2}$$

where W is the internal strain energy volume density of the material. We follow with the definition of the first Piola–Kirchhoff stress tensor $\mathbf{P} = \mathbf{F} \cdot \mathbf{S}$, which, unlike $\mathbf{S}$, has a physical meaning and its increments are related to those of the deformation gradient via the first tangent tensor:

$$\Delta\mathbf{P} = \mathbf{R} : \Delta\mathbf{F}, \quad R_{ijkl} = D_{jrls}F_{ir}F_{ks} + S_{jl}\delta_{ik} \tag{3}$$

where $\mathbf{D}$ is the instantaneous tangent stiffness tensor that relates $\mathbf{S}$ and $\mathbf{C}$ by

$$\mathbf{D} = 2\frac{\partial \mathbf{S}}{\partial \mathbf{C}}, \quad D_{ijkl} = 4\frac{\partial^2 \mathrm{W}}{\partial C_{ij}\partial C_{kl}} \tag{4}$$

and δ_{ij} is the Kronecker delta. In order to model transversely isotropic constituents (e.g., carbon fibers or biological tissues), it is necessary to extend the hyperelastic energy function to represent such anisotropic behavior. To this end, Bonet and Burton [38] derived the St. Venant–Kirchhoff (SVK) energy function, which forms a direct generalization of the linear Hooke's law, as a sum of isotropic,

$$\mathrm{W}_{(\mathrm{SVK})}^{(\mathrm{Iso})} = \frac{1}{2}\lambda(\mathrm{tr}(\mathbf{E}))^2 + \mu\mathbf{E} : \mathbf{E} \tag{5}$$

and transversely isotropic parts,

$$\mathrm{W}_{(\mathrm{SVK})}^{(\mathrm{T-Iso})} = [\varphi + \zeta(\mathrm{I}_1 - 3) + \eta(\mathrm{I}_4 - 1)](\mathrm{I}_4 - 1) - \frac{1}{2}\varphi(\mathrm{I}_5 - 1) \tag{6}$$

where $\mathbf{E}$ is the Green–Lagrangian strain tensor $\mathbf{E} = 1/2(\mathbf{C} - \mathbf{I})$. The total strain energy function for this material is given by

$$\begin{aligned}\mathrm{W}_{(\mathrm{SVK})} =& \frac{1}{2}\lambda(\mathrm{tr}(\mathbf{E}))^2 + \mu\mathbf{E} : \mathbf{E} + \\ & [\varphi + \zeta(\mathrm{I}_1 - 3) + \eta(\mathrm{I}_4 - 1)](\mathrm{I}_4 - 1) - \frac{1}{2}\varphi(\mathrm{I}_5 - 1).\end{aligned} \tag{7}$$

In Eqs. (5–7), λ and μ are Lamé constants, and φ, ζ, η are additional transversely isotropic material parameters; all of which can be expressed in terms of the five parameters: E_L, E_T, ν_L, ν_T, and G_L. Here, E_L and ν_L are the longitudinal Young's modulus and Poisson's ratio; E_T and ν_T are the transverse Young's modulus and Poisson's ratio; and G_L is the longitudinal shear modulus. After lengthy manipulations, the resulting expressions are

$$\begin{aligned}\lambda &= \frac{-E_T(\nu_L^2 E_T + E_L\nu_T)}{2E_T\nu_L^2\nu_T + E_L\nu_T^2 + 2\nu_L^2 E_T - E_L}, \\ \mu &= \frac{E_T}{2(1+\nu_T)}, \\ \varphi &= \frac{-2G_L\nu_T + E_T - 2G_L}{2(1+\nu_T)}, \\ \zeta &= -\frac{E_T(E_L\nu_L\nu_T - \nu_L^2 E_T + E_L\nu_L - E_L\nu_T)}{4(2E_T\nu_L^2\nu_T + E_L\nu_T^2 + 2\nu_L^2 E_T - E_L)}, \\ \eta &= \frac{\eta_1 + \eta_2}{8(2E_T\nu_L^2\nu_T + E_L\nu_T^2 + 2E_T\nu_L^2 - E_L)}\end{aligned} \tag{8}$$

with $\eta_1 = -8E_T G_L \nu_L^2\nu_T + E_L^2\nu_T^2 + 2E_L E_T \nu_L\nu_T - 4E_L G_L\nu_T^2 + E_T^2\nu_L^2$, and $\eta_2 = -8\nu_L^2 E_T G_L + 2E_L E_T\nu_L - E_L^2 - E_L E_T + 4E_L G_L$.

These explicit expressions of the SVK energy function allow characterizing a wide range of hyperelastic materials according to the results of standard testing. It should be noted, however, that under compression the stress response of the SVK material starts to rise at a certain applied deformation (see Holzapfel [37]).

In order to model rubber-like materials subjected to appreciable compressive loading, the well-known compressible Mooney–Rivlin hyperelastic strain energy function, Sussman and Bathe [39], is chosen:

$$\mathrm{W}_{(\mathrm{M-R})} = \mathrm{C}_{10}(\mathrm{I}_1' - 3) + \mathrm{C}_{01}(\mathrm{I}_2' - 3) + \frac{\kappa}{2}\left(\sqrt{\mathrm{I}_3} - 1\right)^2 \tag{9}$$

where C_{10}, C_{01}, and κ are material properties, and I_1' and I_2' are the reduced first and second invariants of the right Cauchy–Green deformation tensor defined by

$$\mathrm{I}_1' = \mathrm{I}_1\mathrm{I}_3^{-1/3}, \quad \mathrm{I}_2' = \mathrm{I}_2\mathrm{I}_3^{-2/3}. \tag{10}$$

This isotropic Mooney–Rivlin representation of the hyperelastic material can also be extended to a transversely isotropic function in the same manner as proposed by Bonet and Burton [38] for the SVK model.

The expression for the stress and the tangent stiffness tensors are readily established by evaluating the derivatives of the strain energy, which for $\mathrm{W}_{(\mathrm{SVK})}$, $\mathrm{W}_{(\mathrm{M-R})}$, and the five invariants are given in Appendix A.

2.2 Damage and failure

The hyperelastic materials that are described by the constitutive equations which were presented in Sect. 2.1 behave such that the accumulated energy and the stress increase as the applied deformation increases. This behavior is not realistic since there is a 'point' where the deformation of the material induces internal damage as multiple separations between the material's particles occur at a certain stretch. To address this issue, Volokh [32] suggested modifying the hyperelastic energy function in order to limit the accumulated energy to a specific value. This new modified energy function is given by:

$$\psi = \psi^F - \psi^E \tag{11}$$

where the 'failure energy,' ψ^F, is the energy that describes the full separation between the particles and is defined by:

$$\psi^F = \frac{\phi}{m}\Gamma\left(\frac{1}{m}, 0\right), \tag{12}$$

and the 'elastic energy,' ψ^E, is given by:

$$\psi^E(\mathbf{C}) = \frac{\phi}{m}\Gamma\left(\frac{1}{m}, \frac{\mathrm{W}^m}{\phi^m}\right) \tag{13}$$

where in Eqs. (12–13), Γ is the 'upper incomplete gamma function,' evaluated by:

$$\Gamma(s, x) = \int_x^\infty t^{s-1}\exp(-t)\mathrm{d}t, \tag{14}$$

The expressions given in Eqs. (11–14) are the generalization of the original form of the energy limiters proposed by Volokh in [31], which allows the representation of additional failure modes. As described in Fig. 1, the modified energy, ψ, is limited by the value of ϕ, and the resulting uniaxial stress–stretch curve drops to a zero-stress level according to the sharpness which is controlled by the parameter m.

Substituting W with ψ in Eqs. (2–4), the modified second Piola–Kirchhoff stress tensor's components S_{ij} are

$$S_{ij} = 2\frac{\partial\psi}{\partial C_{ij}} = 2\frac{\partial\psi}{\partial \mathrm{W}}\frac{\partial \mathrm{W}}{\partial C_{ij}} = 2\exp\left(-\frac{\mathrm{W}^m}{\phi^m}\right)\frac{\partial \mathrm{W}}{\partial C_{ij}}, \tag{15}$$

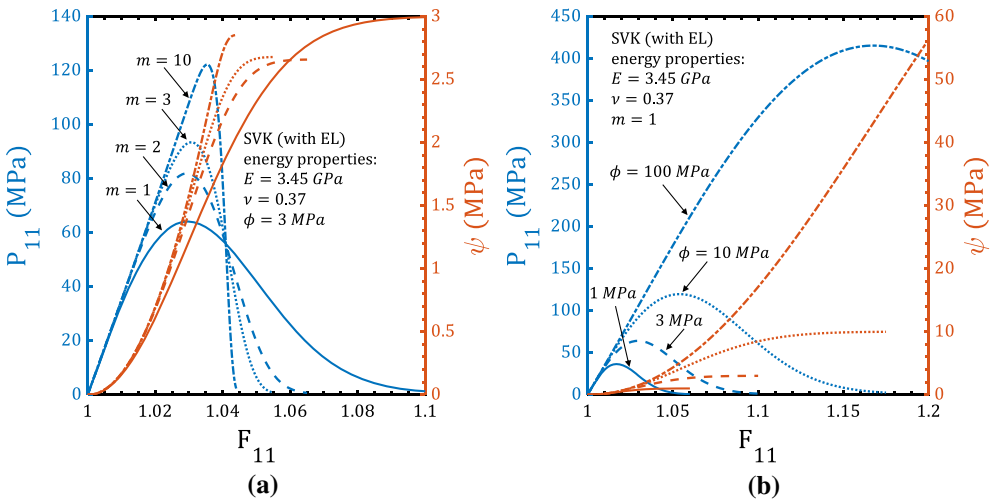

Fig. 1 Effect of the energy limiters approach parameters m (**a**) and ϕ (**b**) on the energy and stress levels of an isotropic St. Venant–Kirchhoff (SVK)

and the resulting components of the modified stiffness tensor **D**, are,

$$\begin{aligned} D_{ijkl} =& 4\frac{\partial^2 \psi}{\partial C_{ij}\partial C_{kl}} \\ =& 4\left\{\frac{\partial^2 \mathrm{W}}{\partial C_{ij}\partial C_{kl}} + \left[\left(-\frac{m}{\phi^m}\right)\mathrm{W}^{(m-1)}\frac{\partial \mathrm{W}}{\partial C_{ij}}\frac{\partial \mathrm{W}}{\partial C_{kl}}\right]\right\}\exp\left(-\frac{\mathrm{W}^m}{\phi^m}\right) \end{aligned} \tag{16}$$

from which the tangent tensor **R** can be established by employing Eq. (3). It should be noted that in the absence of the limiter, $\phi \to \infty$, the resulting expressions in Eq. (16) are reduced to Eq. (4).

3 Finite strain parametric HFGMC micromechanics

In the present Section, a micromechanics theory is presented, which is capable of predicting the global behavior of composites undergoing large deformations. This micromechanical theory is a generalization of the HFGMC to a non-orthogonal discretization of RUCs. In particular, this theory is also capable of predicting the elastic field distributions in the various composite's constituents. Furthermore, the inclusion of the energy limiter, which is described in the previous Section provides the ability to incorporate damage with the applied loading on the composite. The PHFGMC formulation presented in this Section allows the modeling of a composite with doubly periodic microstructure such as continuous fiber-reinforced composites and layered materials. In addition, the proposed version of the PHFGMC enforces a generalized plane-strain state which will be discussed in the following Subsections.

3.1 Tangential constitutive equations

Consider a fiber-reinforced unidirectional composite with periodic microstructure in which the continuous fibers are oriented in the X_Δ direction, as seen in Fig. 2a. A cross section of the composite's RUC is discretized into an arbitrary number of quadrilateral subcells, as seen in Fig. 2b. The finite deformation of the present doubly periodic composite is described with respect to the initial local coordinates in the $Y_2 - Y_3$ plane. The equations of the PHFGMC micromechanical model are formulated with respect to the parametric **r** domain, such that each quadrilateral subcell's physical space (Fig. 2c) is represented by a square-shaped subcell (Fig. 2d). The mapping between these two domains is achieved by employing a linear transformation as follows:

$$\begin{aligned} \mathbf{Y}(r_2, r_3) &= \sum_{k=1}^{4} H_k(r_2, r_3)\mathbf{Y}^{(k)}, \\ H_1 &= \frac{1}{4}(1-r_2)(1-r_3), \quad H_2 = \frac{1}{4}(1+r_2)(1-r_3), \\ H_3 &= \frac{1}{4}(1+r_2)(1+r_3), \quad H_4 = \frac{1}{4}(1-r_2)(1+r_3) \end{aligned} \tag{17}$$

where $\mathbf{Y}(r_2, r_3)$ is the location in the parametric domain, $H_1, .., H_4$ are the bilinear mapping shape functions which depend on the parametric coordinates in the $r_2 - r_3$ plane, and $\mathbf{Y}^{(1)}, .., \mathbf{Y}^{(4)}$ are the locations of the subcell's four vertices in the physical microscale domain. By using the parametric coordinates, the incremental displacement vector of each arbitrary subcell β in the doubly periodic RUC is expanded as

$$\begin{aligned} \Delta\mathbf{u}^{(\beta)} =& \Delta\mathbf{u}^{0,(\beta)} + \Delta\mathbf{w}_0^{(\beta)} \\ &+ \frac{1}{2}\left(\Delta\mathbf{w}_2^{(\beta)} - \Delta\mathbf{w}_4^{(\beta)}\right)r_2 + \frac{1}{2}\left(\Delta\mathbf{w}_3^{(\beta)} - \Delta\mathbf{w}_1^{(\beta)}\right)r_3 \\ &+ \frac{1}{4}\left(\Delta\mathbf{w}_2^{(\beta)} + \Delta\mathbf{w}_4^{(\beta)} - 2\Delta\mathbf{w}_0^{(\beta)}\right)\left(3{r_2}^2 + r_2 r_3 - 1\right) \\ &+ \frac{1}{4}\left(\Delta\mathbf{w}_1^{(\beta)} + \Delta\mathbf{w}_3^{(\beta)} - 2\Delta\mathbf{w}_0^{(\beta)}\right)\left(3{r_3}^2 + r_2 r_3 - 1\right) \end{aligned} \tag{18}$$

where $\Delta\mathbf{u}^{0,(\beta)} \equiv \Delta\mathbf{F}^0 \cdot \mathbf{X}$ is the externally far-field displacement vector as specified by the applied deformation gradient $\Delta\mathbf{F}^0$ at the macroscale location **X**, and the unknown microvariables, $\Delta\mathbf{w}_\mathrm{i}$, i = 0 − 4 are determined

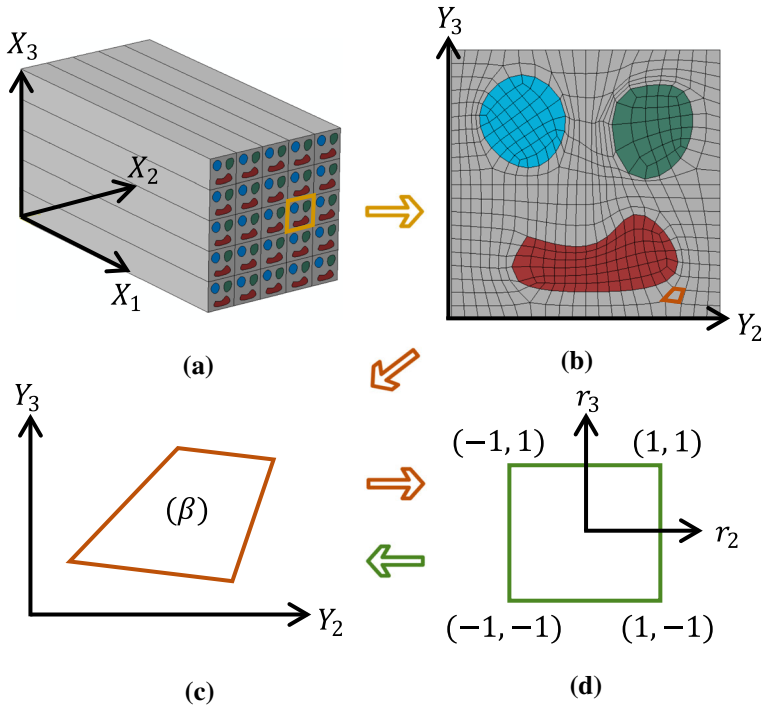

Fig. 2 Schematic drawing of a composite with a repeating geometrical pattern (**a**), a doubly periodic RUC discretization to subcells (**b**), coordinates and geometry in the physical domain of the subcell (**c**), and coordinates and geometry in the parametric domain of the subcell (**d**)

from the governing equations and continuity conditions of PHFGMC. The specific displacement polynomial in Eq. (18), that represents the fluctuations within each subcell, is a modification of the Legendre functions, which can easily enforce orthogonality. The non-modified Legendre functions were previously introduced for the fluctuation in the HFGMC model, and their modification was proposed by Haj-Ali and Aboudi to allow relating each microvariable to an average face value of the subcell (see [19]).

The deformation gradient $\Delta\mathbf{F}^{(\beta)}$ is obtained from Eq. (18) as follows:

$$\Delta\mathbf{F}^{(\beta)} = \Delta\frac{\partial\mathbf{u}^{0,(\beta)}}{\partial\mathbf{X}} + \Delta\frac{\partial\tilde{\mathbf{u}}^{(\beta)}}{\partial\mathbf{Y}} = \Delta\frac{\partial(\mathbf{F}^0\cdot\mathbf{X})}{\partial\mathbf{X}} + \Delta\frac{\partial\tilde{\mathbf{u}}^{(\beta)}}{\partial\mathbf{r}}\cdot\frac{\partial\mathbf{r}}{\partial\mathbf{Y}} \tag{19}$$

where the fluctuation displacement increment $\Delta\tilde{\mathbf{u}}^{(\beta)}$ is given by

$$\begin{aligned}\Delta\tilde{\mathbf{u}}^{(\beta)} \equiv{}& \Delta\mathbf{w}_0^{(\beta)}\\ &+\frac{1}{2}\left(\Delta\mathbf{w}_2^{(\beta)}-\Delta\mathbf{w}_4^{(\beta)}\right)r_2+\frac{1}{2}\left(\Delta\mathbf{w}_3^{(\beta)}-\Delta\mathbf{w}_1^{(\beta)}\right)r_3\\ &+\frac{1}{4}\left(\Delta\mathbf{w}_2^{(\beta)}+\Delta\mathbf{w}_4^{(\beta)}-2\Delta\mathbf{w}_0^{(\beta)}\right)(3{r_2}^2+r_2r_3-1)\\ &+\frac{1}{4}\left(\Delta\mathbf{w}_1^{(\beta)}+\Delta\mathbf{w}_3^{(\beta)}-2\Delta\mathbf{w}_0^{(\beta)}\right)(3{r_3}^2+r_2r_3-1).\end{aligned} \tag{20}$$

In the present case of the doubly periodic RUC, the Jacobian matrix of the inverse mapping $\check{\mathbf{J}}^{(\beta)}$ is given by

$$\check{\mathbf{J}}^{(\beta)} \equiv \begin{bmatrix} \frac{\partial r_1}{\partial Y_1} & \frac{\partial r_1}{\partial Y_2} & \frac{\partial r_1}{\partial Y_3} \\ \frac{\partial r_2}{\partial Y_1} & \frac{\partial r_2}{\partial Y_2} & \frac{\partial r_2}{\partial Y_3} \\ \frac{\partial r_3}{\partial Y_1} & \frac{\partial r_3}{\partial Y_2} & \frac{\partial r_3}{\partial Y_3} \end{bmatrix} = \begin{bmatrix} 1 & 0 & 0 \\ 0 & \frac{\partial r_2}{\partial Y_2} & \frac{\partial r_2}{\partial Y_3} \\ 0 & \frac{\partial r_3}{\partial Y_2} & \frac{\partial r_3}{\partial Y_3} \end{bmatrix}. \tag{21}$$

Substituting Eq.(21) into Eq.(19), the partial derivatives of the displacement at the fluctuation field yields the deformation gradient in the form

$$\Delta\mathbf{F}^{(\beta)} = \Delta\mathbf{F}^{0} + \Delta\frac{\partial\tilde{\mathbf{u}}^{(\beta)}}{\partial\mathbf{r}}\cdot\check{\mathbf{J}}^{(\beta)} \equiv \Delta\mathbf{F}^{0} + \Delta\tilde{\mathbf{F}}^{(\beta)}, \tag{22}$$

and from now on, both the deformation gradient tensor $\Delta\mathbf{F}^{(\beta)}$ and the unknown microvariables vector $\Delta\mathbf{w}^{(\beta)}$ are represented in contracted notation as

$$\begin{aligned}\Delta\mathbf{F}^{(\beta)} &= \{\Delta F_{11}\ \ \Delta F_{12}\ \ \Delta F_{13}\ \ \Delta F_{21}\\ &\quad\ \Delta F_{22}\ \ \Delta F_{23}\ \ \Delta F_{31}\ \ \Delta F_{32}\ \ \Delta F_{33}\}^{\mathrm{T},(\beta)}\\ &\equiv \{\Delta F_{1}\ \ \Delta F_{2}\ \ \Delta F_{3}\ \ \Delta F_{4}\\ &\quad\ \Delta F_{5}\ \ \Delta F_{6}\ \ \Delta F_{7}\ \ \Delta F_{8}\ \ \Delta F_{9}\}^{\mathrm{T},(\beta)}\end{aligned} \tag{23}$$

and

$$\begin{aligned}\Delta\mathbf{w}^{(\beta)} &= \{\Delta w_{1_1}\ \ \Delta w_{1_2}\ \ \Delta w_{1_3}\ \ \Delta w_{2_1}\ \ \Delta w_{2_2}\ \ \Delta w_{2_3}\ \ \Delta w_{3_1}\\ &\quad\ \Delta w_{3_2}\ \ \Delta w_{3_3}\ \ \Delta w_{4_1}\ \ \Delta w_{4_2}\ \ \Delta w_{4_3}\ \ \Delta w_{0_1}\ \ \Delta w_{0_2}\ \ \Delta w_{0_3}\}^{\mathrm{T},(\beta)}\\ &\equiv \{\Delta w_{1}\ \ \Delta w_{2}\ \ \Delta w_{3}\ \ \Delta w_{4}\ \ \Delta w_{5}\ \ \Delta w_{6}\ \ \Delta w_{7}\\ &\quad\ \Delta w_{8}\ \ \Delta w_{9}\ \ \Delta w_{10}\ \ \Delta w_{11}\ \ \Delta w_{12}\ \ \Delta w_{13}\ \ \Delta w_{14}\ \ \Delta w_{15}\}^{\mathrm{T},(\beta)}.\end{aligned} \tag{24}$$

With the present contracted notation, the product and double product operators will henceforth be omitted, and the relation between the increments of the deformation gradient and displacement–microvariables vector can be expressed in terms of a rectangular coefficient matrix (9×15) $\mathbf{A}_{\mathrm{w}}^{(\beta)}$ of subcell β in the form,

$$\Delta\tilde{\mathbf{F}}^{(\beta)} = \mathbf{A}_{\mathrm{w}}^{(\beta)}\Delta\mathbf{w}^{(\beta)}, \quad i.e., \quad \Delta\tilde{F}_{i}^{(\beta)} = A_{w_{i,j}}^{(\beta)}\Delta w_{j}^{(\beta)}, \quad i = 1-9, \quad j = 1-15, \tag{25}$$

and the explicit expressions of the coefficient matrix components $A_{w_{i,j}}^{(\beta)}$ are given in Appendix B.

The continuity conditions of the average displacement increments between neighboring subcells and the periodicity conditions of the average displacement increments between subcells located on opposite RUC edges require that

$$\Delta\bar{\mathbf{u}}^{(\beta_k)} = \Delta\bar{\mathbf{u}}^{(\gamma_m)} \tag{26}$$

where β_k and γ_m are the edges of subcell β and γ, respectively, and the average values are calculated for each face using a line-integral on the incremental displacement vector defined previously in Eq. (18).

The PHFGMC micromechanical equations are derived from the equilibrium state of the composite expressed by the balance of energy. To that end, the potential energy of each subcell $\Pi^{(\beta)}$, which evolves the external and internal energies $\Pi_{\mathrm{ext}}^{(\beta)}$, $\Pi_{\mathrm{int}}^{(\beta)}$, is introduced. The two-scale external energy (work) of an arbitrary subcell (β) is defined as follows:

$$\Pi_{\mathrm{ext}}^{(\beta)} \equiv \{\mathbf{I}_{\mathrm{F}^0}^{(\beta)}\ \ \mathbf{I}_{\mathrm{w}}^{(\beta)}\}\begin{Bmatrix}\mathbf{F}^{0}\\ \mathbf{w}^{(\beta)}\end{Bmatrix} = \mathbf{F}^{0,\mathrm{T}}\mathbf{I}_{\mathrm{F}^0}^{(\beta)} + \mathbf{w}^{(\beta),\mathrm{T}}\mathbf{I}_{\mathrm{w}}^{(\beta)}. \tag{27}$$

Here, $\mathbf{I}_{\mathrm{F}^0}^{(\beta)}$ and $\mathbf{I}_{\mathrm{w}}^{(\beta)}$ are the 'internal resisting vectors' of the subcell with respect to the composite's deformation gradient (i.e., macro-remote) and to the constituents' fluctuation (i.e., micro-local) fields, respectively.

The internal energy of the subcell is defined by a volume integral over the subcell's area $V^{(\beta)}$ using the Green–Lagrangian strain tensor, $\mathbf{E}^{(\beta)}$, and the second Piola–Kirchhoff stress tensor, $\mathbf{S}^{(\beta)}$, as

$$\Pi_{\mathrm{int}}^{(\beta)} \equiv \int_{V^{(\beta)}} \mathbf{E}^{(\beta),\mathrm{T}}\mathbf{S}^{(\beta)}\mathrm{d}V. \tag{28}$$

Using the expressions in Eqs. (27, 28), the total potential energy of the subcell is

$$\Pi^{(\beta)} = \int_{V^{(\beta)}} \mathbf{E}^{(\beta),\mathrm{T}}\mathbf{S}^{(\beta)}\mathrm{d}V - \left(\mathbf{F}^{0,\mathrm{T}}\mathbf{I}_{\mathrm{F}^0}^{(\beta)} + \mathbf{w}^{(\beta),\mathrm{T}}\mathbf{I}_{\mathrm{w}}^{(\beta)}\right). \tag{29}$$

The variation of the potential energy with respect to the macro- and micromechanical variables, $\mathbf{F}^0$ and $\mathbf{w}^{(\beta)}$, leads to

$$\int_{V^{(\beta)}} \delta\mathbf{F}^{0,\mathrm{T}}\mathbf{P}^{(\beta)}\mathrm{d}V - \delta\mathbf{F}^{0,\mathrm{T}}\mathbf{I}_{\mathrm{F}^0}^{(\beta)} = \mathbf{0} \tag{30}$$

and

$$\int_{V^{(\beta)}} \delta\mathbf{w}^{(\beta),\mathrm{T}}\mathbf{A}_{\mathrm{w}}^{(\beta),\mathrm{T}}\mathbf{P}^{(\beta)}\mathrm{d}V - \delta\mathbf{w}^{(\beta),\mathrm{T}}\mathbf{I}_{\mathrm{w}}^{(\beta)} = \mathbf{0}. \tag{31}$$

These two equalities follow from the equivalence of variation of internal energy [37],

$$\int_{V^{(\beta)}} \delta\mathbf{E}^{(\beta),\mathrm{T}}\mathbf{S}^{(\beta)}\mathrm{d}V = \int_{V^{(\beta)}} \delta\mathbf{F}^{(\beta),\mathrm{T}}\mathbf{P}^{(\beta)}\mathrm{d}V, \tag{32}$$

and Eqs. (22, 25) which provide

$$\int_{V^{(\beta)}} \delta\mathbf{E}^{(\beta),\mathrm{T}}\mathbf{S}^{(\beta)}\mathrm{d}V = \int_{V^{(\beta)}} \delta\mathbf{F}^{0,\mathrm{T}}\mathbf{P}^{(\beta)}\mathrm{d}V + \int_{V^{(\beta)}} \delta\mathbf{w}^{(\beta),\mathrm{T}}\mathbf{A}_{\mathrm{w}}^{(\beta),\mathrm{T}}\mathbf{P}^{(\beta)}\mathrm{d}V. \tag{33}$$

Due to the arbitrariness of the variation presented in Eqs. (30–31), the following equivalences are gained:

$$\mathbf{I}_{\mathrm{F}^0}^{(\beta)} = \int_{V^{(\beta)}} \mathbf{P}^{(\beta)}\mathrm{d}V \tag{34}$$

and

$$\mathbf{I}_{\mathrm{w}}^{(\beta)} = \int_{V^{(\beta)}} \mathbf{A}_{\mathrm{w}}^{(\beta),\mathrm{T}}\mathbf{P}^{(\beta)}\mathrm{d}V. \tag{35}$$

The equilibrium equations of the whole RUC are achieved by balancing the internal resisting vectors from all subcells and by assembling each contribution according to its continuity and periodicity relations with other subcells according to Eq. (26). This procedure is explicitly elaborated in Appendix C, and generates the following overall set of equations:

$$\begin{bmatrix} \mathbf{K}_{\mathrm{ww}} & \mathbf{K}_{\mathrm{wF}^0} \\ \mathbf{K}_{\mathrm{F}^0\mathrm{w}} & \mathbf{K}_{\mathrm{F}^0\mathrm{F}^0} \end{bmatrix} \begin{Bmatrix} \Delta\mathbf{w} \\ \Delta\mathbf{F}^0 \end{Bmatrix} = \begin{Bmatrix} \mathbf{0} \\ \mathbf{0} \end{Bmatrix} \tag{36}$$

where $\Delta\mathbf{F}^0$ is determined by the externally applied loading, and as established in Appendix C, Eq. (C.7), the subcell's 'stiffness matrices' are given as

$$\begin{aligned} \mathbf{K}_{\mathrm{ww}}^{(\beta)} &= \int_{V^{(\beta)}} \mathbf{A}_{\mathrm{w}}^{(\beta),\mathrm{T}}\mathbf{R}^{(\beta)}\mathbf{A}_{\mathrm{w}}^{(\beta)}\mathrm{d}V, \\ \mathbf{K}_{\mathrm{wF}^0}^{(\beta)} &= \int_{V^{(\beta)}} \mathbf{A}_{\mathrm{w}}^{(\beta),\mathrm{T}}\mathbf{R}^{(\beta)}\mathrm{d}V, \\ \mathbf{K}_{\mathrm{F}^0\mathrm{w}}^{(\beta)} &= \int_{V^{(\beta)}} \mathbf{R}^{(\beta)}\mathbf{A}_{\mathrm{w}}^{(\beta)}\mathrm{d}V, \\ \mathbf{K}_{\mathrm{F}^0\mathrm{F}^0}^{(\beta)} &= \int_{V^{(\beta)}} \mathbf{R}^{(\beta)}\mathrm{d}V. \end{aligned} \tag{37}$$

The solution of the above PHFGMC equations provides the microvariables $\Delta\mathbf{w}^{(\beta)}$ of all subcells from which the deformation gradients and stresses can be determined. Furthermore, this allows the computation of the current mechanical concentration tensors $\mathbf{G}^{(\beta)}$ of the subcells that relate the externally applied deformation gradient $\Delta\mathbf{F}^0$ to the local ones:

$$\Delta\mathbf{F}^{(\beta)} = \mathbf{G}^{(\beta)}\Delta\mathbf{F}^0. \tag{38}$$

The computational technique to calculate the components of the concentration tensors is by applying a 'dummy' $\Delta\mathbf{F}^0$ for each of the deformation gradient tensor's components and solving the PHFGMC equations for each

one of them. These 'dummy' tensors contain the value of 1 in one of its components, and 0 in the rest. The solution for each component will provide the appropriate single column in $\mathbf{G}^{(\beta)}$. Using this result, and in conjunction with the definition of the average stress in the composite over the volume of the whole RUC, V_{RUC}, expressed in terms of the average stress in the subcells, the following relation is obtained:

$$\Delta\mathbf{P}^0 = \frac{1}{V_{RUC}} \sum_{\beta=1}^{N_{sc}} \int_{V^{(\beta)}} \Delta\mathbf{P}^{(\beta)} \mathrm{d}V \tag{39}$$

where N_{sc} is the total number of subcells in the RUC. Hence, the effective instantaneous stiffness tensor of the composite can be established as (see [24])

$$\mathbf{R}^* = \frac{1}{V_{RUC}} \int_{V_{RUC}} \mathbf{R}^{(\beta)}\mathbf{G}^{(\beta)} \mathrm{d}V = \frac{1}{V_{RUC}} \sum_{\beta=1}^{N_{sc}} \int_{V^{(\beta)}} \mathbf{R}^{(\beta)}\mathbf{G}^{(\beta)} \mathrm{d}V \tag{40}$$

so that the homogenized constitutive equation of the composite can be represented in the form:

$$\Delta\mathbf{P}^0 = \mathbf{R}^* \Delta\mathbf{F}^0. \tag{41}$$

This equation which involves the current first tangent tensor $\mathbf{R}^*$ is integrated in a stepwise manner to obtain the global stress $\mathbf{P}^0$ of the composite at a given value of the deformation $\mathbf{F}^0$.

3.2 Incremental-iterative numerical scheme

In the case of a homogeneous material, the microstructure fluctuation vanished, and therefore there is no need to solve the PHFGMC system of equations (Eq. (36)). This is in contradistinction with the analysis of composites, as discussed in the following.

The mechanical constitutive and governing equations defined in the previous Section allow to compute the mechanical response of the composite in an incremental scheme. However, at a certain point where the effective first tangent stiffness tensor $\mathbf{R}^*$ has negative values, convergence might be at risk since the system of equations is not positive definite. This will occur whenever a subcell exhibits energies above its critical level, and thus, its tangential relation, $\Delta\mathbf{P}^{(\beta)} = \mathbf{R}^{(\beta)}\Delta\mathbf{F}^{(\beta)}$, reaches the 'softening-negative' region (see Fig. 1). Therefore, although the embedded energy limiters theory provides the PHFGMC model the ability to describe the damage of the phases, it does not address the failure of each material point without using negative values in the stiffness matrix. To that end, a new incremental-iterative scheme for the finite strain PHFGMC is proposed in Fig. 3.

The proposed algorithm goes as follows. Firstly, the PHFGMC analysis initiates the total mechanical tensors and vectors of all subcells, $F_{ij}^{(\beta)} = \delta_{ij}$, $P_{ij}^{(\beta)} = 0$, $u_i^{(\beta)} = 0$, and of the composite, $F_{ij}^0 = \delta_{ij}$, $P_{ij}^0 = 0$ (Fig. 3, block 1); Secondly, the incremental scheme begins (Fig. 3, block 2) with the initiation of the incremental tensors and vectors of all subcells, $\Delta F_{ij}^{(\beta)} = 0$, $\Delta P_{ij}^{(\beta)} = 0$, $\Delta u^{(\beta)} = 0$, and of the composite, $\Delta F_{ij}^0 = 0$, $\Delta P^0 = 0$ (Fig. 3, block 3).

At each increment q, following a failure of any subcell, a progressive failure analysis will begin if any other subcell is close to reaching its critical failure energy value. This is determined by setting two energy margins, namely $\psi_{C_L}^{(\beta)}$ and $\psi_{C_H}^{(\beta)}$, where, for example, they can be 95 and 99 percent of its critical energy value. In the case of $\psi_{C_L}^{(\beta)} < \psi^{(\beta)} < \psi_{C_H}^{(\beta)}$, an iterative scheme is initiated while keeping the remote load at the same value (Fig. 3, block 4), and only these subcells will be allowed to fail during the iteration. For a similar methodology to solve a mechanical progressive failure analysis for composites at infinitesimal strains, see Aboudi et al [9, chapter 7].

The first step in each iteration n is to initiate the trail tensors (Fig. 3, block 5) for each subcell, which will henceforth appear with a hat. The trail deformation gradient and the trail first Piola–Kirchhoff tensors, $\hat{\mathbf{F}}^{(\beta)}$ and $\hat{\mathbf{P}}^{(\beta)}$, are defined as follows (Fig. 3, query 1):

$$\hat{\mathbf{F}}^{(\beta),(q,n)} = \begin{cases} \hat{\mathbf{F}}^{(\beta),(q,n-1)}, & \psi^{(\beta),(q-1)} > \psi_{C_L}^{(\beta)} \\ \mathbf{F}^{(\beta),(q-1)}, & \psi^{(\beta),(q-1)} \leq \psi_{C_L}^{(\beta)} \end{cases},$$

$$\hat{\mathbf{P}}^{(\beta),(q,n)} = \begin{cases} \hat{\mathbf{P}}^{(\beta),(q,n-1)}, & \psi^{(\beta),(q-1)} > \psi_{C_L}^{(\beta)} \\ \mathbf{P}^{(\beta),(q-1)}, & \psi^{(\beta),(q-1)} \leq \psi_{C_L}^{(\beta)} \end{cases}, \tag{42}$$

After setting these values, the trail instantaneous stiffness matrices, $\hat{\mathbf{R}}^{(\beta)}$, are calculated for all subcells (Fig. 3, block 6). In the case that the energy level of one of the allowable subcells to fail has now reached an energy level larger than the critical higher bound, $\psi_{C_H}^{(\beta)}$, then its stiffness is reduced to a relatively low value as (Fig. 3, query 2),

$$\hat{\mathbf{R}}^{(\beta),(q,n)} = \begin{cases} \epsilon \cdot \mathbf{R}^{(\beta)}\left(\mathbf{F}^{(\beta),(q=0)}\right), & \psi^{(\beta),(q)} > \psi_{C_H}^{(\beta)} \\ \hat{\mathbf{R}}^{(\beta)}\left(\mathbf{F}^{(\beta),(q,n)}\right), & \psi^{(\beta),(q)} \leq \psi_{C_H}^{(\beta)} \end{cases} \tag{43}$$

where ϵ usually has a very small non-dimensional value ($\sim$0.0001). The resulting stiffness matrices allow to assemble the left-hand side (LHS) of the PHFGMC overall set of equations (see Appendix C), thus provides the trail concentration matrices, $\hat{\mathbf{G}}^{(\beta)}$, as described in Eq. (38), and the effective stiffness tensor of the whole composite, $\hat{\mathbf{R}}^{*}$ (Fig. 3, blocks 7-8).

In the framework of this research, the proposed PHFGMC block diagram is aimed for a stress-driven scheme, where, for example, the analyses can enforce a uniaxial tensile stress state or an in-plane shear stress state. Toward that goal, the trail incremental remote deformation gradient, $\Delta\hat{\mathbf{F}}^{0}$, is calculated to address the specific applied stress state, and follows by the assembly of the right-hand side (RHS) of the PHFGMC overall set of equations (see Appendix C and Fig. 3, block 9). The solution of the PHFGMC equations provides the trail microvariables, $\Delta\hat{\mathbf{w}}^{(\beta)}$, and thus the trail deformation gradient tensor's components, $\Delta\hat{\mathbf{F}}^{(\beta)}$, via Eq. (25) (Fig. 3, block 10). This further allows the calculation of the total deformation gradient tensor's components $\hat{\mathbf{F}}^{(\beta)}$, and the current energy level of each subcell $\psi^{(\beta)}$.

In the case of $\psi^{(\beta)} > \psi_{C_H}^{(\beta)}$ (Fig. 3, query 3), the subcell is indicated as a failed material point, and it will not be able to carry any stress, and its incremental and total first Piola–Kirchhoff stress tensor's components $\Delta\hat{\mathbf{P}}^{(\beta)}$, $\hat{\mathbf{P}}^{(\beta)}$ will be reduced to zero. However, in order to restrain the remote applied stress state, the released stresses from the failed subcell β that were not in the applied direction must dissipate within the composite to the active subcells γ.

To that end, the total stress tensor of the failed subcell is divided into two parts as

$$\hat{\mathbf{P}}^{(\beta),(q,n)} = \mathbf{P}^{(\beta-0)} + \mathbf{P}^{(\beta-\gamma)} \tag{44}$$

where, for example, if the required applied remote stress is a uniaxial state at the Y_1-axis, the explicit terms of $\mathbf{P}^{(\beta-0)}$ and $\mathbf{P}^{(\beta-\gamma)}$ are

$$\begin{aligned} \mathbf{P}^{(\beta-0)} &= \{P_{11} \quad 0 \quad 0 \quad 0 \quad 0 \quad 0 \quad 0 \quad 0 \quad 0\}^{(\beta),(q,n),T}, \\ \mathbf{P}^{(\beta-\gamma)} &= \{0 \quad P_{12} \quad P_{13} \quad P_{21} \quad P_{22} \quad P_{23} \quad P_{31} \quad P_{32} \quad P_{33}\}^{(\beta),(q,n),T}. \end{aligned} \tag{45}$$

Following this separation, the first update of the trail incremental and total stress tensors takes place according to

$$\begin{aligned} \Delta\hat{\mathbf{P}}^{(\beta),(q,n)} &= \begin{cases} \mathbf{0}, & \psi^{(\beta),(q,n)} > \psi_{C_H}^{(\beta)} \\ \hat{\mathbf{R}}^{(\beta),(q,n)}\Delta\hat{\mathbf{F}}^{(\beta),(q,n)}, & \psi^{(\beta),(q-1)} \leq \psi_{C_H}^{(\beta)} \end{cases}, \\ \hat{\mathbf{P}}^{0,(q,n)} &= \begin{cases} \hat{\mathbf{P}}^{0,(q-1)} + \hat{\mathbf{R}}^{*}\Delta\hat{\mathbf{F}}^{0,(q,n)} - \frac{V^{(\beta)}}{V_{RUC}}\mathbf{P}^{(\beta-0)}, & \psi^{(\beta),(q,n)} > \psi_{C_H}^{(\beta)} \\ \hat{\mathbf{P}}^{0,(q-1)} + \hat{\mathbf{R}}^{*}\Delta\hat{\mathbf{F}}^{0,(q,n)}, & \psi^{(\beta),(q,n)} \leq \psi_{C_H}^{(\beta)} \end{cases}, \\ \hat{\mathbf{P}}^{(\beta),(q,n)} &= \begin{cases} \mathbf{0}, & \psi^{(\beta),(q,n)} > \psi_{C_H}^{(\beta)} \\ \hat{\mathbf{P}}^{(\beta),(q-1)} + \hat{\mathbf{R}}^{(\beta)}\Delta\hat{\mathbf{F}}^{(\beta),(q,n)}, & \psi^{(\beta),(q,n)} \leq \psi_{C_H}^{(\beta)}. \end{cases} \end{aligned} \tag{46}$$

The second update of the tensors is established by dissipating $\mathbf{P}^{(\beta-\gamma)}$ within the RUC, which effectively modifies the mechanical state of the remaining active subcells to enforce a new global equilibrium of the

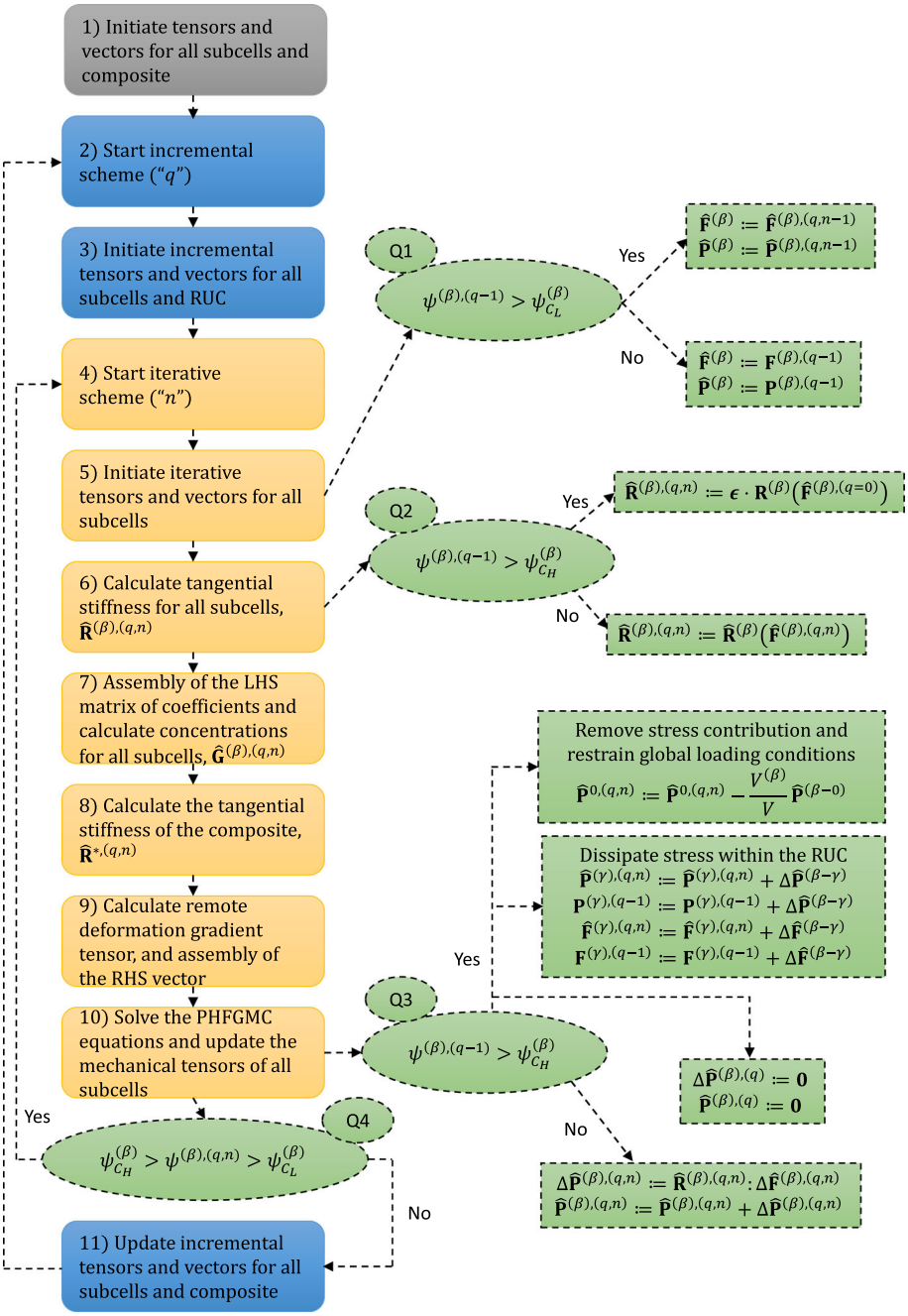

Fig. 3 Finite strain PHFGMC incremental-iterative progressive failure algorithm

microstructure. The effective compliance matrix of the composite allows calculating an effective remote deformation gradient tensor that generates the required dissipated stress as

$$\mathbf{F}^{(\beta-\gamma)} = \mathbf{R}^{*,-1}\frac{\mathrm{V}^{(\beta)}}{\mathrm{V}_{\mathrm{RUC}}}\mathbf{P}^{(\beta-\gamma)}. \tag{47}$$

Using these values to reassemble the RHS of the PHFGMC equations (see Appendix C), and solving them, provides the second update of the active subcell's tensors as

$$\hat{\mathbf{P}}^{(\gamma),(q,n)} = \hat{\mathbf{P}}^{(\gamma),(q,n)} + \Delta\mathbf{P}^{(\beta-\gamma)},$$

$$\begin{aligned}\mathbf{P}^{(\gamma),(q-\Delta)} &= \mathbf{P}^{(\gamma),(q-\Delta)} + \Delta\mathbf{P}^{(\beta-\gamma)},\\ \hat{\mathbf{F}}^{(\gamma),(q,n)} &= \hat{\mathbf{F}}^{(\gamma),(q,n)} + \Delta\mathbf{F}^{(\beta-\gamma)},\\ \mathbf{F}^{(\gamma),(q-\Delta)} &= \mathbf{F}^{(\gamma),(q-\Delta)} + \Delta\mathbf{F}^{(\beta-\gamma)}.\end{aligned} \tag{48}$$

At this stage, the iterative scheme is finished, unless there is any subcell that did not fail but reached an energy value that is larger than the predetermined lower bound, $\psi_{C_L}^{(\beta)}$. In this case, a new iteration will take place (Fig. 3, query 4), and the final iterative solution will be amended in the incremental tensors and arrays of the subcells and RUC (Fig. 3, block 11).

4 Applications

The finite strain PHFGMC micromechanics, in conjunction with damage and failure, which was discussed in Sect. 3, together with the algorithm in Fig. 3, are employed to generate the mechanical response of several wavy-layered composites at both the macro- and microscales. The present Section demonstrates the various capabilities of this algorithm to predict the failure evolution of both theoretically and commonly used composite materials. These wavy-layered composites, which are caused by manufacturing faults, are represented by RUCs created using a mesh generator as described in Fig. 4. The overall height, H, and thickness, L, of the RUC, and the fiber volume fraction, v_f, that determine the diameter of the fiber, d_f, are presented in Fig. 4a, where the fiber region is in light gray, and the matrix region is in dark gray. The fiber's waviness is described by a sin function: $u_2^0(Y_2, Y_3) = u_2^I(Y_2)sin(2\pi Y_3/H)$, where the amplitude is changed throughout the thickness of the RUC. The amplitude varies from a constant waviness value in the fiber region, $u_2^I = u_{2f}^I$, to a waviness at the matrix region that is reduced from $u_2^I = u_{2m}^I = u_{2f}^I$ at the fiber–matrix interface, to $u_2^I = u_{2m}^I = 0$ at the RUC's edges, as seen in Fig. 4b, c, by:

$$u_2^I(Y_2) = \begin{cases} \frac{u_{2f}^I}{\frac{1}{2}d_m} Y_2, & 0 \le Y_2 < \frac{1}{2}d_m \\ u_{2f}^I, & \frac{1}{2}d_m \le Y_2 < \frac{1}{2}d_m + d_f \\ \frac{u_{2f}^I}{\frac{1}{2}d_m}(L - Y_2), & \frac{1}{2}d_m + d_f \le Y_2 \le L. \end{cases} \tag{49}$$

The fiber region is partitioned into 8 subcells with equal thickness, x_f, and the matrix region (right and left subregions marked in $(1/2)d_m$ in Fig. 4b) is partitioned into 14 subcells with degraded thickness from the highest, x_m at the edge of the RUC, to the lowest $(1/\alpha)x_m$ at the fiber–matrix interface, according to a thickness-scale parameter $\alpha = 3$ as presented in Fig. 4c.

The proposed algorithm of the PHFGMC was coded in Fortran for in-house use, which allows a stand-alone mode of solving micromechanical problems. The analyses of the composites presented in this Section were performed using an 8-core Intel® i7 processor. The overall system of equations of the PHFGMC was solved using the parallel direct sparse solver (Pardiso) subroutine, which is available by Intel® oneAPI math kernel library (MKL) [40,41]. For a characteristic wavy-layered RUC that was created using the mesh generator described above with an overall of 1760 subcells, the number of unknowns is 10587 (after static condensation), which takes the PHFGMC several minutes to solve 300 increments of loading with a varied number of iterations (a maximum of 20) in each increment according to the evolving failure pattern. Furthermore, in the present investigation, all of the area-integrals were evaluated by using the numerical integration at the 2 by 2 Gaussian quadrature rule (see [42] for additional information on numerical integration).

4.1 Effect of axis of symmetry orientation of the interfacial layer

In order to illustrate the effect of the anisotropic constituents' orientation on the composite response, let us consider a case in which a third phase is added between the stiff and soft layers of Fig. 4a, see Fig. 5a. The orientation of the axis of symmetry of this interphase layer varies between the Y_2- and Y_3-axes. To that end, the interphase is modeled as a carbon nanotubes/epoxy (CNT/epoxy) layer, where several methods are established to direct the orientation of CNTs as mechanical and magnetic fabrication processes, which highly affect the effective response of the CNT/epoxy composite materials (see [43] and [44], for example). The

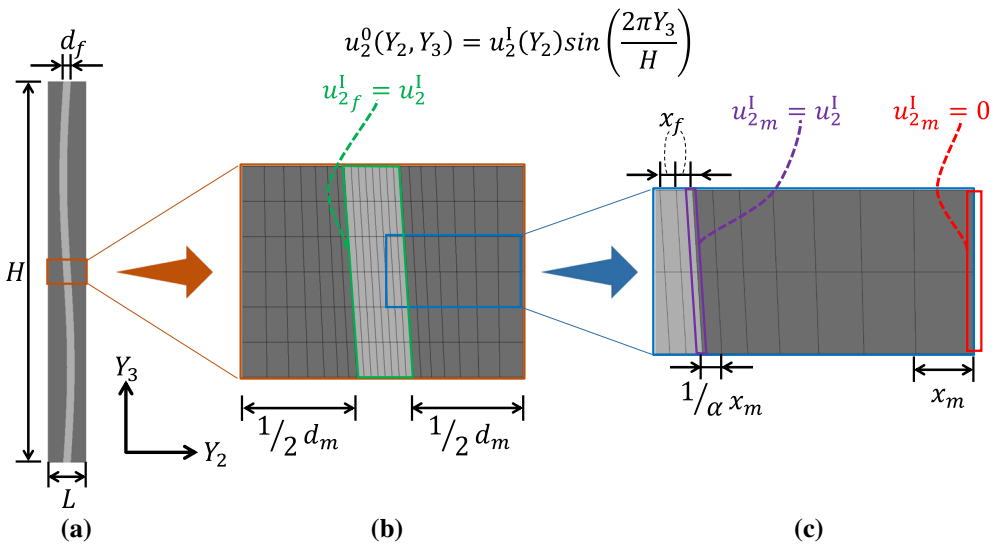

Fig. 4 Wavy-layered repeating unit cell (RUC) with height H and thickness L (**a**). Typical discretization, thickness, and waviness of the stiff (fiber) and soft (matrix) regions (**b**, **c**)

Table 1 Mechanical properties for the stiff (fiber), intermediate (interphase), and soft (matrix) regions for the micromechanical PHFGMC analyses presented in Fig. 5

Stiff region (carbon fiber): transversely isotropic SVK, Eq. (7)					
Mechanical properties	$E_L^{\check{f}}$ 276 GPa	$E_T^{\check{f}}$ 16 GPa	$\nu_L^{\check{f}}$ 0.31	$\nu_T^{\check{f}}$ 0.28	$G_L^{\check{f}}$ 15 GPa
Damage properties	$m^{\check{f}}$ 10	$\phi^{\check{f}}$ 30 MPa	$\phi_C^{\check{f}}$ 12 MPa		
Intermediate region (fiber–matrix interphase): transversely Isotropic SVK, Eq. (7)					
Mechanical properties	$E_L^{\check{i}}$ 20.0 GPa	$E_T^{\check{i}}$ 3.50 GPa	$\nu_L^{\check{i}}$ 0.30	$\nu_T^{\check{i}}$ 0.40	$G_L^{\check{i}}$ 1.30 GPa
Damage properties	$m^{\check{i}}$ 2	$\phi^{\check{i}}$ 2.00 MPa	$\phi_C^{\check{i}}$ 0.8 MPa		
Soft region (epoxy matrix): isotropic SVK, Eq. (5)					
Mechanical properties	$E_L^{\check{m}}$ 3.45 GPa	$E_T^{\check{m}}$ 3.45 GPa	$\nu_L^{\check{m}}$ 0.37	$\nu_T^{\check{m}}$ 0.37	$G_L^{\check{m}}$ 1.26 GPa
Damage properties	$m^{\check{m}}$ 1	$\phi^{\check{m}}$ 3.00 MPa	$\phi_C^{\check{m}}$ 1.25 MPa		

wavy-layered composites RUC considered herein is a 5% carbon fiber with a 34% of CNTs/epoxy interphase layer. Both of these regions are modeled by the transversely isotropic SVK constitutive relation (Eq. (7)), and the remaining 61% epoxy region is modeled by the isotropic SVK constitutive relation (Eq. (5)) with the mechanical properties presented in Table 1. Corresponding to Fig. 5, the superscripts $\check{f}$, $\check{i}$, and $\check{m}$ in Table 1 refer to the properties of the fiber, interphase, and matrix subcells, respectively, where all three energies include the damage effect of the energy limiters approach. In the present application, the orientation of the axis of symmetry of the CNT/epoxy region is changed from $\theta = 0°$, which coincides with the positive Y_2 direction, to $\theta = 180°$. The axis of symmetry at the fiber region is generally parallel to the Y_3 direction, as each subcell is slightly rotated according to its initial deflection (see, for example, the right-hand side of Fig. 5a that the subcells are slightly deflected to the left).

The overall response of the composites to a uniaxial compressive longitudinal stress state is presented on the left-hand side of Fig. 5a, and the microscale compressive longitudinal stress, $-P_{33}^{(\beta)}$, field distribution within the RUC is presented in Fig. 5b. It can be clearly observed that the effective stiffness and strength of the composite are significantly affected by the change of the interphase orientation. Furthermore, due to the symmetry of the RUC's geometry, any change in the orientation from 90° by $-\theta$ or by $+\theta$ provides exactly the same effective response, which is weaker and softer than the fully aligned interphase at the Y_3 direction.

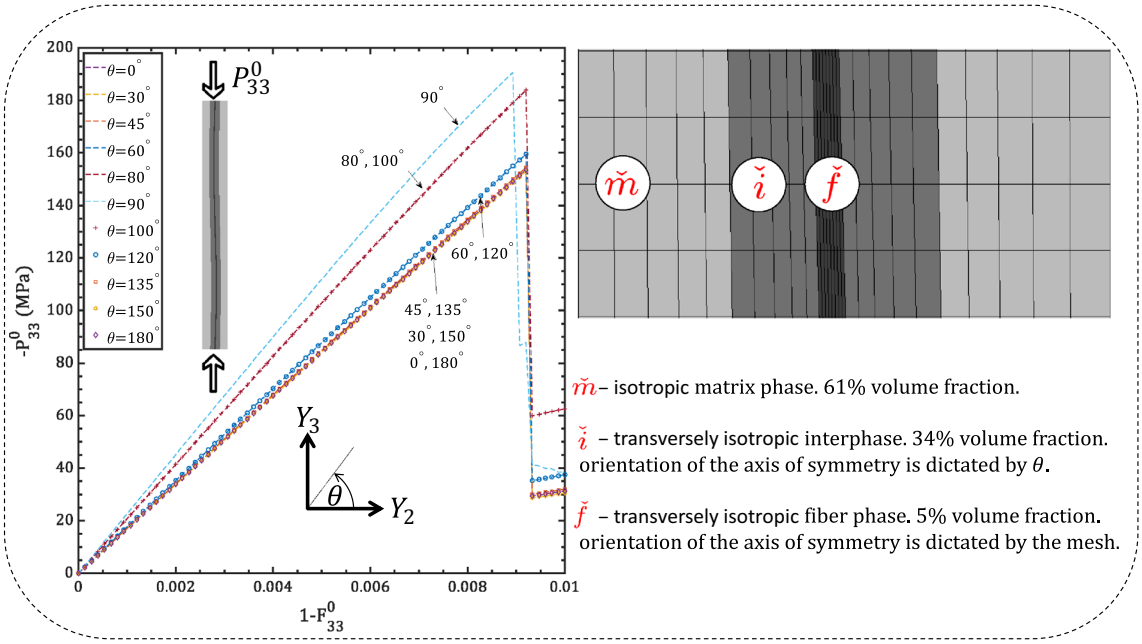

(a)

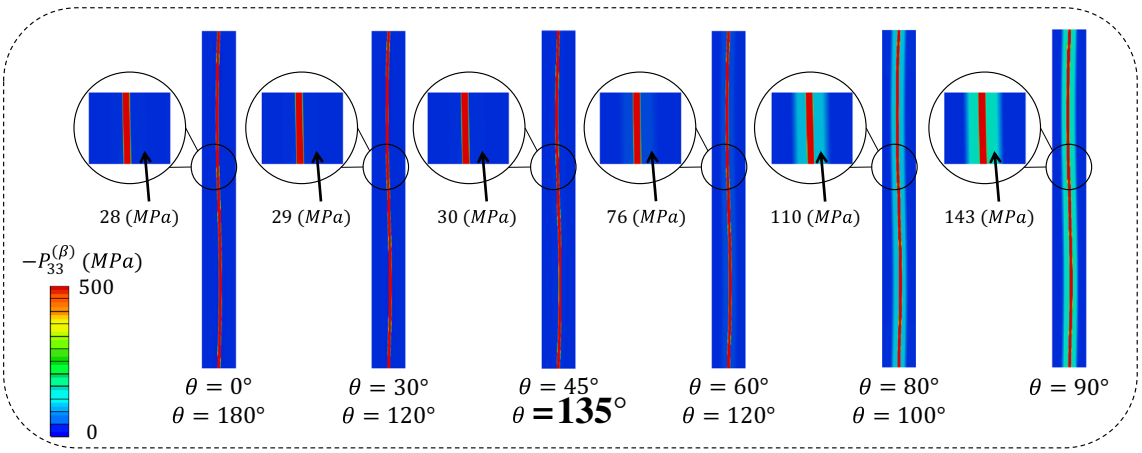

(b)

Fig. 5 Wavy-layered composite with three phases at uniaxial compressive stress state. The effect of the controlled orientation θ of the interphase's axis of symmetry on the overall response is presented on the left side of (**a**), and the geometrical dimensions are presented on the right side of (**a**). The microscale (fluctuation) compressive stress field distributions, at $1 - F^0_{33} = 0.008$ are presented in (**b**). The constituent's mechanical properties are given explicitly in Table 1

In addition, the initial alignment rotation from the Y_3-axis generates lower compressive stress values at the interphase region as shown in Fig. 5b. Thus, the values were reduced from ∼143 MPa for the 90° RUC to ∼28 MPa for the 0° and 180° RUCs (see zoom-in views for each orientation in Fig. 5b). It should be noted that very similar results were observed for RUCs with orientation in the range of $0° - 45°$ or in the range of $135° - 180°$, where it appears that only when the alignment of the interphase is closer to the Y_3-axis rather than to the Y_2 axis (e.g., $45° < \theta < 135°$) the interphase will appreciatively contribute to the overall strength and stiffness (see Fig. 5a). This is also apparent in the microscale distribution of the stress fields within the RUCs (see Fig. 5b), where the stress in the ranges of $0° - 45°$ or $135° - 180°$ and the stress at the interphase region were very similar to those in the epoxy matrix region. In conclusion, it is possible to enhance the stiffness and strength of the composite by controlling the axis of symmetry orientation of the fiber–matrix interphase layer.

Table 2 Mechanical properties for the stiff (fiber) and soft (matrix) regions for the micromechanical PHFGMC analyses presented in Figs. 6 and 7

Stiff region (Carbon fiber): transversely Isotropic SVK, Eq. (7)					
Mechanical properties	$E_L^{\check{f}}$ 276 GPa	$E_T^{\check{f}}$ 16 GPa	$\nu_L^{\check{f}}$ 0.31	$\nu_T^{\check{f}}$ 0.28	$G_L^{\check{f}}$ 15 GPa
Damage properties	$m^{\check{f}}$ 10	$\phi^{\check{f}}$ 30 MPa	$\phi_C^{\check{f}}$ 12 MPa		
Soft region (Epoxy matrix): Isotropic SVK, Eq. (5)					
Mechanical Properties	$E_L^{\check{m}}$ 3.45 GPa	$E_T^{\check{m}}$ 3.45 GPa	$\nu_L^{\check{m}}$ 0.37	$\nu_T^{\check{m}}$ 0.37	$G_L^{\check{m}}$ 1.26GPa
Damage properties	$m^{\check{m}}$ 1	$\phi^{\check{m}}$ 3.00 MPa	$\phi_C^{\check{m}}$ 1.25 MPa		

4.2 Effect of the composite's RUC architecture

The second application presented herein investigates the effect of the geometrical dimensions of the composite's RUC, including the influence of the waviness on its response. Let the composite be subjected to a compressive longitudinal stress state. Several RUCs, created by using the mesh generator described in Fig. 4, with different geometrical features were considered. The three geometrical features that are presently examined are:

a) the ratio between the RUC's overall height and the fiber's diameter H/d_f,
b) the ratio between the initial deflection amplitude and the thickness of the RUC u_{2f}^I/L,
c) and the fiber volume fraction d_f/L.

The orientation of the axis of symmetry of the fiber phase was calculated differently for each subcell, as described in Sect. 4.1, and the mechanical properties for both phases are given in Table 2.

For the initial amplitude ratio u_{2f}^I/L, the results are presented in Fig. 6a for the range between a very small value $u_{2f}^I/L = 10^{-6}$ (teal color) to $u_{2f}^I/L = 10^{-1}$ (blue color), while the other dimensions were set to $H/d_f = 16.67$ and $d_f/L = 0.6$. It can be clearly observed that the strength of the composite is significantly reduced when the initial amplitude of the prescribed waviness increases. The ultimate compressive stress drops from $\sim$ 1.51 GPa at $u_{2f}^I/L = 10^{-6}$ to $\sim$ 1.21 GPa at $u_{2f}^I/L = 10^{-1}$. In addition, the waviness changes the alignment of the fiber from the Y_3 direction according to its local curvature, causing the fiber's stiffness at this direction to decrease accordingly. Thus, since the fiber's transverse stiffness modulus is much lower than its longitudinal modulus (see Table 2), the effective compressive stiffness of the RUC at the Y_3 direction is also reduced. A similar trend is also observed in Fig. 6b, where six RUCs with different H/d_f were created from a high ratio of $H/d_f = 50.00$ to $H/d_f = 8.33$ with $d_f/L = 0.6$ and $u_{2f}^I/L = 10^{-1}$ for all RUCs. At the highest ratio, the fiber is nearly aligned with the Y_3-axis as opposed to the lowest H/d_f ratio where the initial fiber rotation is meaningful, thus the effective strength and stiffness of the composite are much lower (the effective strength changes from $\sim$ 1.45 GPa at $H/d_f = 50.00$ to $\sim$ 1.00 GPa at $H/d_f = 8.33$).

The third comparison was performed for six RUCs with different fiber volume fractions $d_f/L = 0.2 - 0.7$ with the other dimension set as $H/d_f = 50.00$ and waviness of $u_{2f}^I/L = 10^{-1}$, see Fig. 6c. For all these six cases, the strength and stiffness of the composites are affected only by the constituents' volume fraction, and the intuitively expected trend of higher strength and stiffness values for higher fiber volume fraction is obtained.

In order to better understand the progressive failure on the overall response, the analysis for the case of $H/d_f = 41.67$, which is shown in Fig. 6b, is chosen to demonstrate the failure progression and stress distribution at the vicinity of the failure events. In Fig. 7a, there are three points of interest marked as A, B, and C. The compressive longitudinal stress, $-P_{33}^{(\beta)}$, and the in-plane shear stress, $P_{32}^{(\beta)}$, are presented in Fig. 7b, c, respectively. In addition, the severity of the failure at each point of interest is shown in Fig. 7d such that an intact subcell is colored in light gray (the energy level in all of the integration points is below the critical value, thus failure equals 0), and an entirely failed subcell is colored in black (the energy level in all of the integration points is above the critical value, thus failure equals 1). These detailed results at the microscale correlate to the overall response presented in Fig. 7a, where at point A, the RUC is just before the initiation of failure, and all of the subcells still carry the remote load. Point B in Fig. 7d shows that the failure initiates in the RUC at the highly compressed regions at the fiber–matrix interface. Hence, the necessary modifications of values of

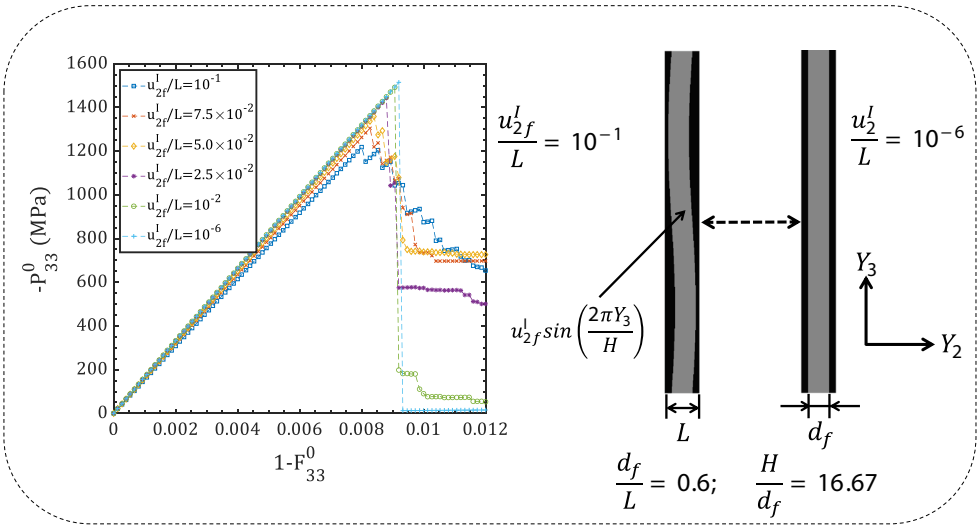

(a)

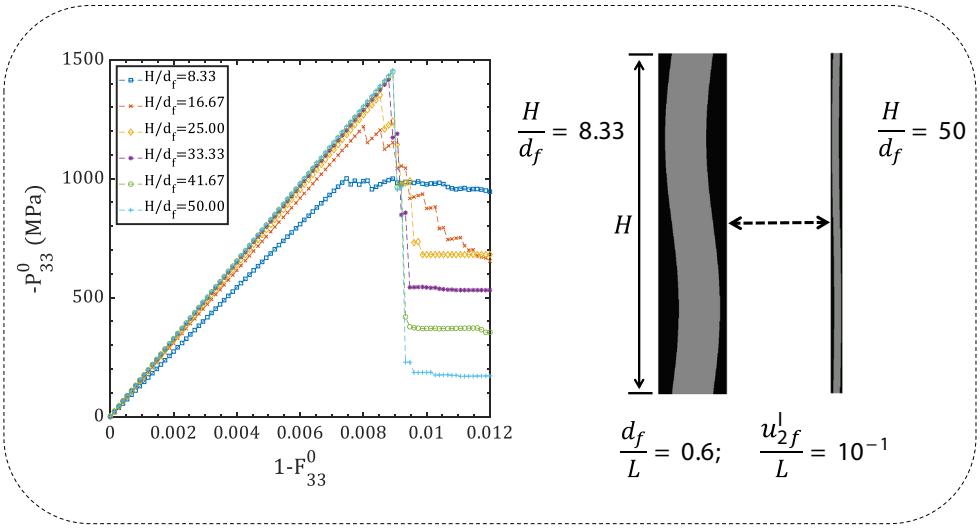

(b)

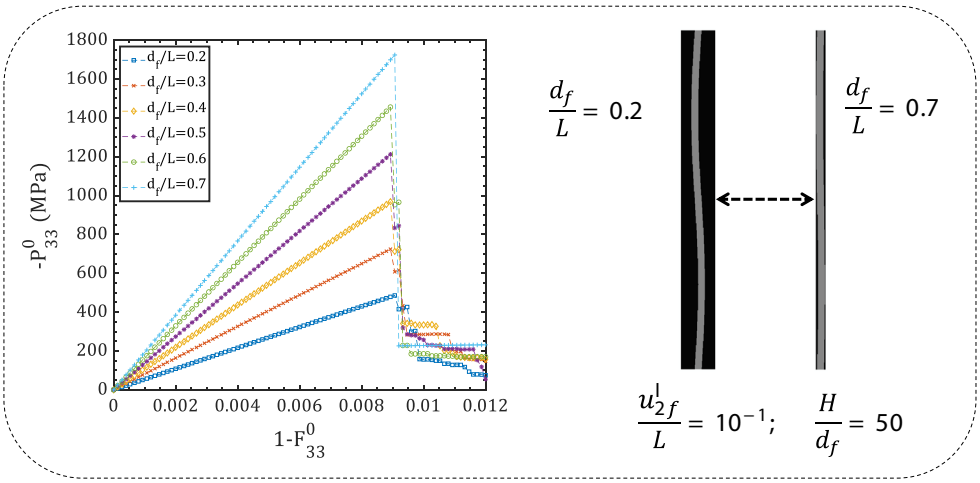

(c)

Fig. 6 Finite strain PHFGMC results for wavy-layered composites at longitudinal compressive stress state modeled by several RUCs with different geometrical architecture. Subfigures **a**–**c**) present the effect of the amplitude of the waviness, the effect of the overall thickness-height ratio, and the effect of the fiber volume fraction on the effective strength and stiffness of the composite, respectively. Constituent's mechanical properties are given explicitly in Table 2

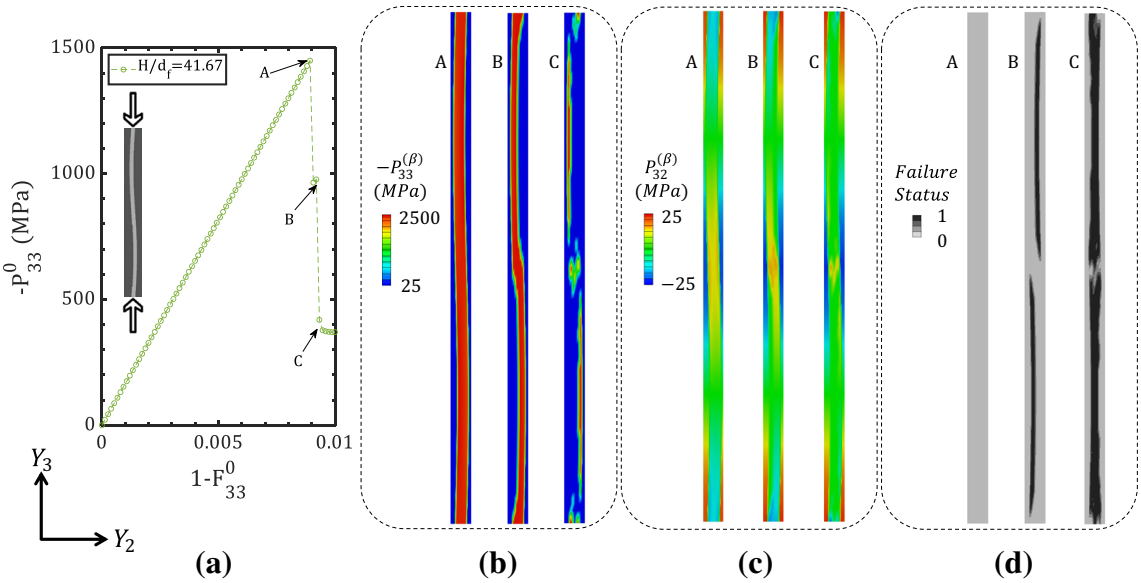

Fig. 7 Finite strain PHFGMC results of the compressive response of wavy-layered composite with indications on three major failure events marked as A, B, and C are presented in (**a**), the compressive longitudinal stress field distribution $P_{33}^{(\beta)}$ is presented in (**b**), the in-plane shear stress field distribution $P_{23}^{(\beta)}$ is presented in (**c**), and the failure status of each subcell (from 0—intact to 1—fully failed) is presented in (**d**)

the deformation gradient and the Piola–Kirchhoff stress tensors components are performed according to the algorithm that is shown in Fig. 3. The reduction of the stress values in the intact subcells to the failed subcells is shown in Fig. 7b, c. Next, when failure progresses to a more severe state, point C, almost all subcells in the fiber region have reached failure, and their stress levels are now negligible, as observed in Fig. 7b–d. This emphasizes the correlation between the reduction of stress at the macroscale, which was decreased by 70% from point A, and the region of entirely failed subcells at the microscale.

In summary, it has been shown that by changing the geometrical dimension of the RUC, the curvature of the fiber changes, thus forming high stress concentration areas at the fiber–matrix interface leading to failure of the constituents in that region. This further leads to a stress dissipation caused by the failure of the considered region till a catastrophic failure of the entire RUC occurs. Moreover, the waviness of the fiber generates a rotation of the fiber's axis of symmetry from the Y_3-axis. This results in a reduction of the macroscale strength and stiffness of the layered composite, especially when the fiber's waviness is more pronounced.

4.3 Effect of the anisotropy of the reinforcing layer

The third application focuses on the effect of the reinforcing layer's (fiber) isotropic and anisotropic properties. Toward this goal, let us consider two epoxy matrix composite systems. In the first one, isotropic boron fibers reinforce an epoxy matrix (BFRP), whereas the second one is strengthened by transversely isotropic high modulus-carbon fibers (HM-CFRP). The elastic and failure properties of all three materials (epoxy, boron, and carbon) are given in Table 3. The two composite systems are modeled by considering several RUCs having different geometrical dimensions and waviness. As discussed in the following, two representative RUCs were generated for the three geometrical ratios that were examined in Sect. 4.2 of u_{2f}^I/L, H/d_f, and d_f/L. These RUCs are subjected to a uniaxial stress state, and their overall responses are shown in the left-hand side of Fig. 8a–c. Since the longitudinal elastic modul: $E_L^{\check{f}}$, of the boron and carbon fibers are quite similar, but not equal, the compressive stress in each plot was normalized by its corresponding fiber modulus as $-P_{33}^0/E_L^{\check{f}}$.

By examining Fig. 8a–c, it can be observed that the main difference between the two systems is the relative reduction of the strength values of the considered two RUCs. In Fig. 8a, the increase in waviness amplitude from $u_{2f}^I/L = 10^{-6}$ to 5×10^{-2} results in a drop of ~11% in strength value for the BFRP composite (2.16

Table 3 Mechanical properties for the stiff (fiber) and soft (matrix) regions for the micromechanical PHFGMC analyses presented in Fig. 8

Stiff region (high modulus carbon fiber): transversely isotropic SVK, Eq. (7)					
Mechanical properties	$E_L^{\check{f}}$	$E_T^{\check{f}}$	$\nu_L^{\check{f}}$	$\nu_T^{\check{f}}$	$G_L^{\check{f}}$
	379 GPa	6.21 GPa	0.20	0.25	7.59 GPa
Damage properties	$m^{\check{f}}$	$\phi^{\check{f}}$	$\phi_C^{\check{f}}$		
	5	32 MPa	19 MPa		
Stiff region (Boron fiber): isotropic SVK, Eq. (5)					
Mechanical properties	$E_L^{\check{f}}$	$E_T^{\check{f}}$	$\nu_L^{\check{f}}$	$\nu_T^{\check{f}}$	$G_L^{\check{f}}$
	400 GPa	400 GPa	0.20	0.20	166.67 GPa
Damage properties	$m^{\check{f}}$	$\phi^{\check{f}}$	$\phi_C^{\check{f}}$		
	5	32 MPa	19 MPa		
Soft region (Epoxy matrix, for both composites): Isotropic SVK, Eq. (5)					
Mechanical properties	$E_L^{\check{m}}$	$E_T^{\check{m}}$	$\nu_L^{\check{m}}$	$\nu_T^{\check{m}}$	$G_L^{\check{m}}$
	3.45 GPa	3.45 GPa	0.37	0.37	1.26 GPa
Damage properties	$m^{\check{m}}$	$\phi^{\check{m}}$	$\phi_C^{\check{m}}$		
	1	3.00 MPa	1.25 MPa		

GPa to 1.93 GPa), whereas a decrease of only ∼4% was observed for the HM-CFRP system (2.10 GPa to 2.02 GPa).

Figure 8b, on the other hand, compares different height to diameter ratios, the decrease in the strength is ∼21% for the BFRP composite (2.11 GPa to 1.67 GPa), and about ∼11% for the HM-CFRP system (2.08 GPa to 1.85 GPa). This decrease in the strength in both systems can be attributed to the reduction of H/d_f from 50.0 to 16.67, which effectively localized the curvature of the fibers.

Consider next the effect of the fiber volume fraction d_f/L variation on the composite response which is presented in Fig. 8c. Here, the reduction in strength was quite similar in both systems. Thus, the strengths of the composites of 0.7 fiber volume fraction are 2.47 GPa and 2.43 GPa for the BFRP and HM-CFRP, respectively. For the composites with 0.2 fiber volume fraction, on the other hand, the strengths are 0.68 GPa and 0.70 GPa for these two systems. Hence the respective drops in strength were ∼72% and ∼71% for the BFRP and HM-CFRP UDs. The present results indicate that the relative reduction of strength is far more sensitive to the change and localization of the fiber's curvature rather than to the fiber volume fraction regardless of whether the fiber is isotropic or not.

Further understanding of the failure behavior of these composites is achieved by the investigation of the resulting micromechanical fields of the PHFGMC. To that end, the longitudinal stress distribution at $1 - F_{33}^0 = 0.008$ and the failure initiation are presented in the middle and right-hand side of Fig. 8a–c (note that the failure initiation is shown at the first occurrence of failure independently for each RUC, and the stress fields are presented at the same deformation for all cases). In each group, the RUCs are ordered by their type and predicted strength from left to right as BFRP with higher strength, HM-CFRP with higher strength, BFRP with lower strength, and HM-CFRP with lower strength.

The presented stress distributions in Fig. 8a–c indicate that the stress concentration is more prominent near the most significant curvature of the fibers. It should be noted that this distribution was especially pronounced for the BFRP system in the sense that it directly affected the failure initiation patterns as the area of failure is highly localized. This phenomenon correlates with the macroscale behavior of the composites, since when the failure initiates at a prior stage of the loading, it leads to lower strength prediction for the BFRPs.

It is possible to explain the difference between the strength and failure initiation prediction of the considered two systems by the high values of the boron fiber's transverse modulus and the in-plane shear modulus as compared to those of the HM-carbon fiber. Thus, composites reinforced with the carbon fiber exhibit a more gradual increase in stiffness from the matrix region to the fiber ($E_T^{\check{f}}/E_T^{\check{m}} \approx 2$ and $G_L^{\check{f}}/G_L^{\check{m}} \approx 6$, rather than for the BFRP systems $E_T^{\check{f}}/E_T^{\check{m}} \approx 116$ and $G_L^{\check{f}}/G_L^{\check{m}} \approx 132$). The high contrasts can induce higher stress concentrations especially in areas where the fibers are significantly curved. This explains the results in Fig. 8a, in which $u_{2_f}^I/L = 10^{-6}$ and the fibers are almost fully aligned with the Y_3-axis, no stress concentration is exhibited at the fiber–matrix interface, and the failure initiation is catastrophic for both composite systems.

To conclude this Section, it was observed that for isotropic fibers the strength reduction of the composite was significant when the waviness either increased or localized. On the other hand, for transversely isotropic

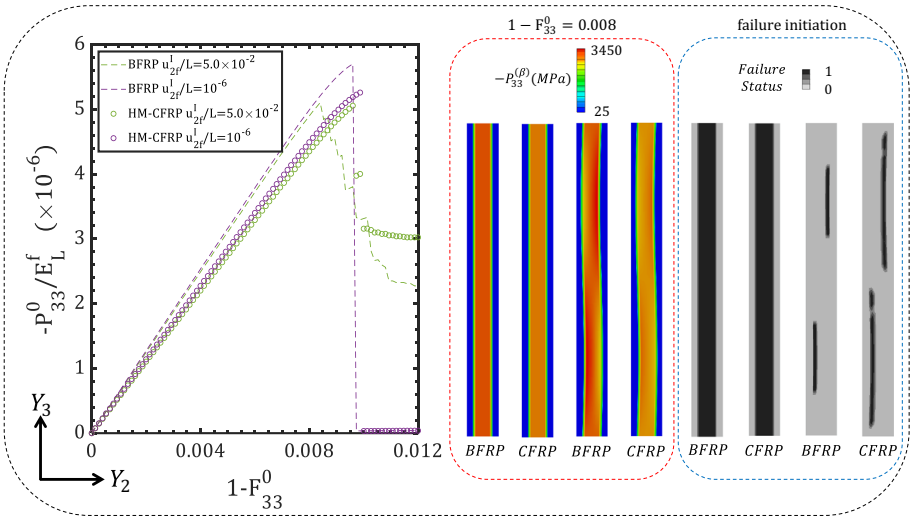

(a)

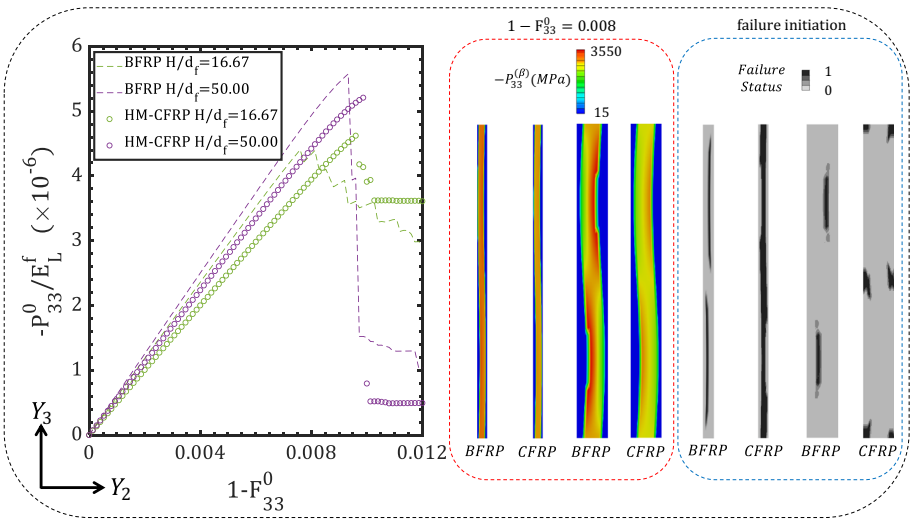

(b)

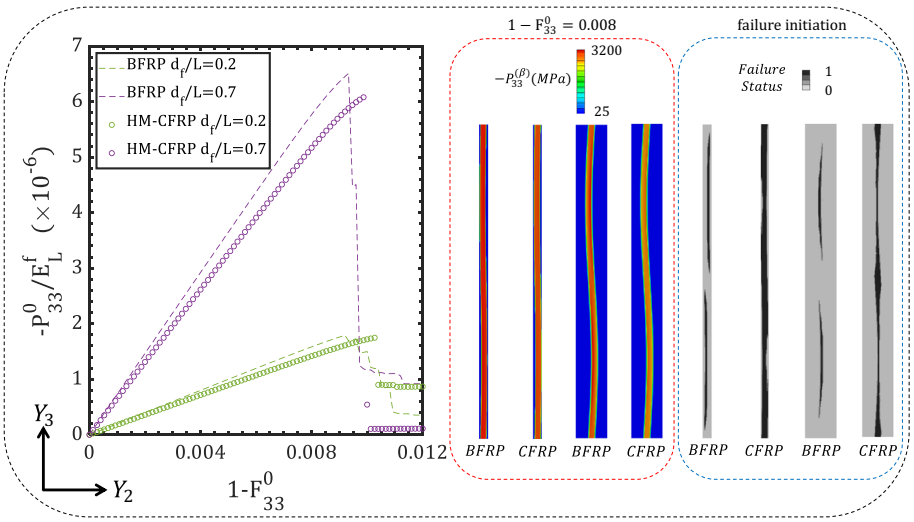

(b)

Fig. 8 Finite strain PHFGMC results of the fiber's anisotropy effect on the composite's strength and stiffness (on the left-hand side), and on the stress distribution and failure initiation at the microscale (on the right-hand side). The constituent's mechanical properties are given explicitly in Table 3

Table 4 Mechanical properties for the stiff (fiber) and soft (matrix) regions for the micromechanical PHFGMC analyses presented in Fig. 9 and calibrated according to the IM7/977-3 composite material system experimental results that were reported by Clay and Knoth [45]

Stiff region (IM7 carbon fiber): Transversely Isotropic SVK, Eq. (7)					
Tensile properties					
Mechanical Properties	$E_L^{\check{f}}$ 276 GPa	$E_T^{\check{f}}$ 13 GPa	$\nu_L^{\check{f}}$ 0.31	$\nu_T^{\check{f}}$ 0.28	$G_L^{\check{f}}$ 15 GPa
Damage properties	$m^{\check{f}}$ 10	$\phi^{\check{f}}$ 80 MPa	$\phi_C^{\check{f}}$ 60 MPa		
Compressive properties					
Mechanical properties	$E_L^{\check{f}}$ 225 GPa	$E_T^{\check{f}}$ 13 GPa	$\nu_L^{\check{f}}$ 0.31	$\nu_T^{\check{f}}$ 0.28	$G_L^{\check{f}}$ 15 GPa
Damage properties	$m^{\check{f}}$ 1	$\phi^{\check{f}}$ 120 MPa	$\phi_C^{\check{f}}$ 18 MPa		
Soft region (977-3 Epoxy matrix): Isotropic SVK, Eq. (5)					
Tensile properties					
Mechanical properties	$E_L^{\check{m}}$ 3.7 GPa	$E_T^{\check{m}}$ 3.7 GPa	$\nu_L^{\check{m}}$ 0.37	$\nu_T^{\check{m}}$ 0.37	$G_L^{\check{m}}$ 1.35 GPa
Damage properties	$m^{\check{m}}$ 2	$\phi^{\check{m}}$ 2.8 MPa	$\phi_C^{\check{m}}$ 1.3 MPa		
Compressive properties					
Mechanical Properties	$E_L^{\check{m}}$ 3.7 GPa	$E_T^{\check{m}}$ 3.7 GPa	$\nu_L^{\check{m}}$ 0.37	$\nu_T^{\check{m}}$ 0.37	$G_L^{\check{m}}$ 1.35 GPa
Damage Properties	$m^{\check{m}}$ 2	$\phi^{\check{m}}$ 18.0 MPa	$\phi_C^{\check{m}}$ 6.0 MPa		

These fitted properties are also used in Fig. 10

fibers, the failure of the composite is more catastrophic, but at the same time, its strength was less sensitive to the geometrical dimensions changes. Furthermore, it was observed that both systems showed similar sensitivity to the changes of fiber volume fraction, and that the strength of the composite is more affected by the isotropy of the wavy fiber rather than its volume fraction.

4.4 Comparison with experiments

As a practical application presented in this paper, the proposed PHFGMC micromechanical analysis is employed to generate failure envelopes of the commonly used polymeric composite system: IM7/977-3 UD CFRP. A highly detailed experimental program on this composite was previously performed by the Air Force Research Laboratory (AFRL) and published by Clay and Knoth [45]. In this Subsection, the calibration of the constituents' elastic and failure properties, and the ability of the PHFGMC to generate initial failure envelopes for different tension–compression states, are demonstrated.

The calibration of the mechanical properties for both constituents was performed by: (i) utilizing the manufacturer tensile data of the IM7 fiber; (ii) the experimental results [45] of the unidirectional coupons in compression and tension in both 0° and 90° directions; and (iii) by detecting additional values from published data on this specific material system. The detailed calibration process is presented in Appendix D. A summary of the material properties for both constituents at compressive and tensile states is given in Table 4. The resulting calibration process of stress–strain plots obtained from the calibration is presented in Fig. 9. The compressive and tensile longitudinal responses of the composite are presented in Fig. 9a, b, respectively, and the compressive and tensile transverse responses of the composite are presented in Fig. 9c, d, respectively.

The obtained properties are implemented in the PHFGMC to demonstrate the generation of the initial failure envelopes in the $P_{22}^0 - P_{33}^0$ stress plane. To that end, the RUC of the composite, with the geometrical dimensions of $u_{2_f}^I/L = 2.5 \times 10^{-2}$, $H/d_f = 15$, and $d_f/L = 0.65$, is subjected to 32 biaxial stress states (see Appendix D for additional information about the determination of the three geometrical ratios). For each point on the envelope, the ratio between the incremental deformation gradient components is enforced (for an equally biaxial loading, for example, $\Delta F_{22}^0/\Delta F_{33}^0 = 1$), and the PHFGMC analysis imposed all stress tensor components to be zero, except for the longitudinal and transverse components $P_{33}^0 \neq 0$, $P_{22}^0 \neq 0$, respectively.

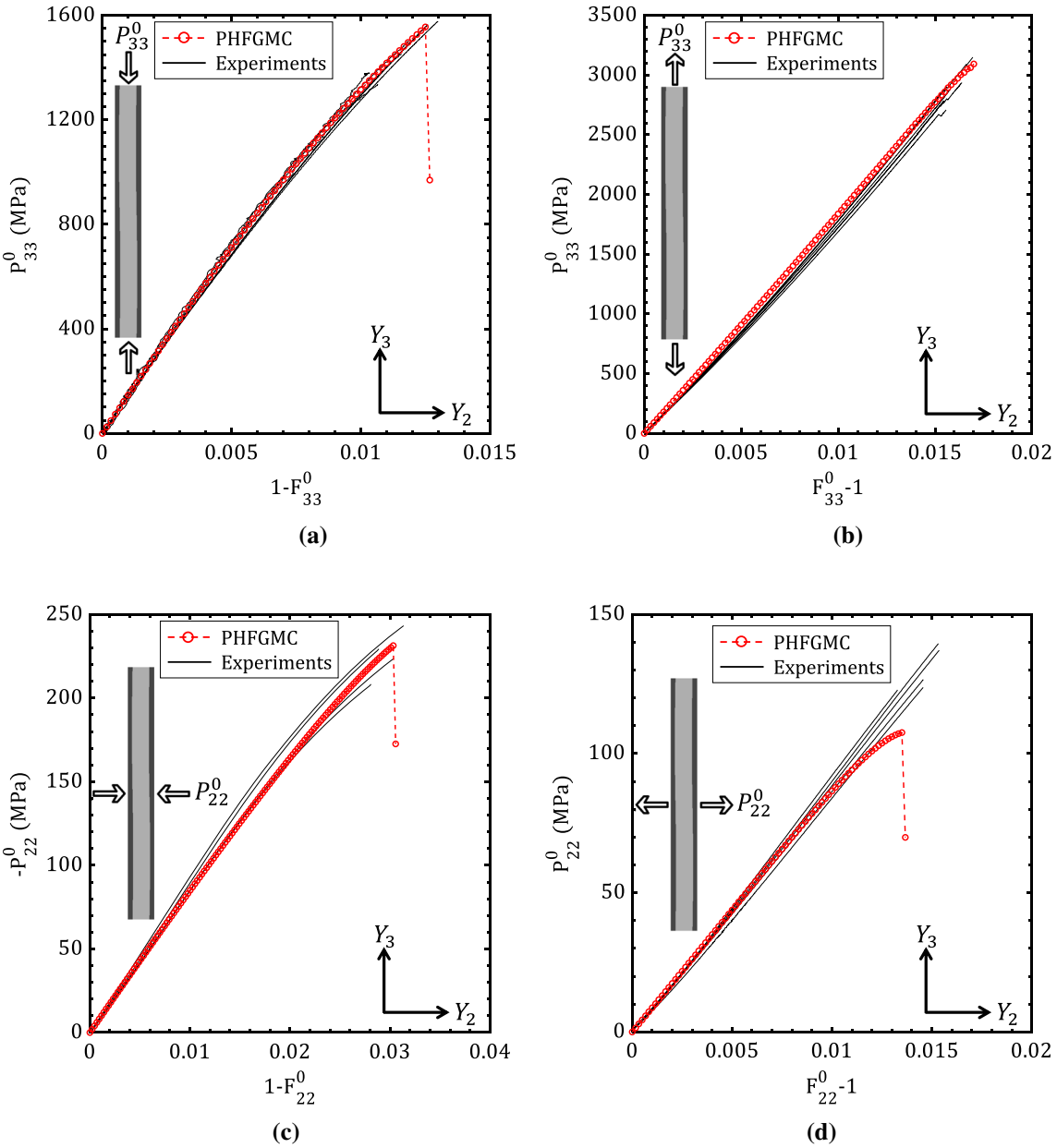

Fig. 9 PHFGMC calibration results for IM7/977-3 CFRP composite system. Longitudinal compressive and tensile responses are presented in (**a**) and (**b**), respectively. Transverse compressive and tensile responses are presented in (**c**) and (**d**), respectively. The constituents' elastic, damage, and failure properties are presented in Table 4. The experimental results, that were obtained by Clay and Knoth [45], were explicitly reported by Bogdanor and Oskay [46], Godines et al. [47], among others. Subfigure **a** contains three additional replicates that were tested during this research in the exact same method as reported in [45]

The analysis is terminated once any subcell reaches its critical energy value, and therefore indicates the initiation of a failure in the composite.

During the analysis, each of the subcells' deformation state is checked to determine whether it is in a 'compressive' or 'tensile' state by the sign of the pseudo-fourth invariant I_4. For example, the fiber longitudinal elastic modulus is given by (see Table 4),

$$E_L^{\check{f}} = \begin{cases} 276 \text{ GPa}, & \mathrm{I}_4{}^{(\beta),(q,n)} \geq 1 \ \{\text{tensile state}\} \\ 225 \text{ GPa}, & \mathrm{I}_4{}^{(\beta),(q,n)} < 1 \ \{\text{compressive state}\} \end{cases}. \tag{50}$$

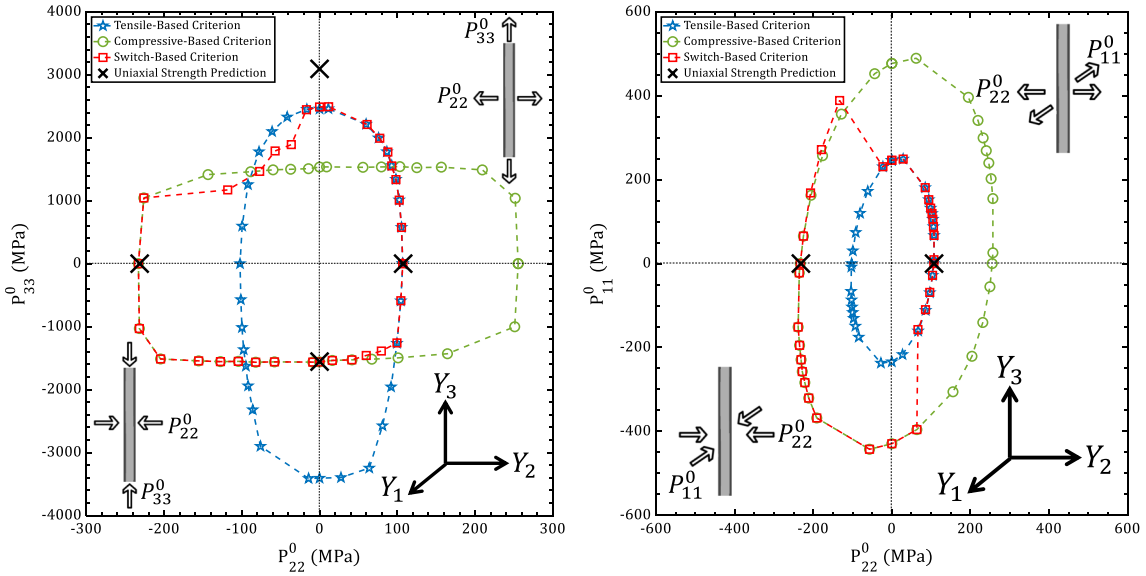

Fig. 10 PHFGMC initial failure envelopes prediction for IM7/977-3 carbon/epoxy composite system. The constituents' elastic, damage, and failure properties are given in Table 4

It should be noted that this tension–compression criterion was proposed by Holzapfel and Ogden [48] to determine the tension–compression state of the fibers for fibrous composites, and a similar switch is also implemented in commercial FEA software as Abaqus [49].

Three initial failure envelopes in the $P^0_{22} - P^0_{33}$ plane are presented in Fig. 10a where each envelope was generated using the properties detailed in Table 4 as follows. (i) Using only the tensile properties in blue, (ii) using only the compressive properties in green, and (iii) using the tensile–compressive switch as described in Eq. (50) in red. In addition, the ultimate uniaxial stress values denoted by black X-shaped markers and backed out from the experimental results are shown. It can be readily observed that the largest gap between the initial failure and ultimate stress of the composite is obtained for the 0° tensile analysis. This gradual failure is commonly observed during experiments, as the epoxy matrix and the fiber–matrix interface are cracked during the test causing the initial failure event to occur at a lower stage of the loading (the strength of the composite is measured when the fiber cannot carry any further load). For all other 3 uniaxial stress states, the initial failure matched the strength of the composite, which is typical for 90° tensile/compressive experiments where the matrix usually carries most of the load and the composite is prone to a sudden failure, and also for the 0° compressive experiments where microbuckling causes catastrophic failure at once.

By comparing the three envelopes, it is clear that the red-envelope that uses the tension–compression criterion coincides in the 1st quarter with the blue-envelope which is based on the tensile properties. In the 3rd quarter however, the red-envelope coincides with the green-envelope that is generated by using the compressive properties of the fiber and matrix.

In the 2nd and 4th quarters, the composite is subjected to a tensile–compressive state, and therefore the PHFGMC predicts the initial failure using both the tensile and compressive properties, and consequently the red-envelope does not necessarily track either the tensile-state or compressive-state envelopes.

A similar trend was observed in the failure envelopes generated by the proposed PHFGMC in the $P^0_{11} - P^0_{22}$ plane, as shown in Fig. 10b. As expected, the initial failure values of the composite in both directions are much lower than the predicted values of the composite in the fiber (longitudinal) direction Y_3 (see Fig. 10a). However, as expected, the composite's initial failure values differ between the 'layered' direction Y_1 to the transverse direction Y_2. In particular, during the deformation of the composite in the Y_1-axis, the fiber–matrix interface, which is the weakest area in the composite, carries less load compared to the deformation state in the Y_2-axis, thus the initiation of failure is postponed.

In conclusion, these results highlight the ability of the PHFGMC to correctly predict the overall response of the composite while employing the tensile–compressive criterion at the microlevel.

Table 5 Mechanical properties for the stiff (fiber) and soft (matrix) regions for the micromechanical PHFGMC analyses presented in Figs. 11 and 12

Stiff region (Nylon fiber): Isotropic SVK, Eq. (5)					
Tensile properties					
Mechanical properties	$E_L^{\check{f}}$	$E_T^{\check{f}}$	$\nu_L^{\check{f}}$	$\nu_T^{\check{f}}$	$G_L^{\check{f}}$
	22.04 MPa	22.04 MPa	0.25	0.25	8.82 MPa
Damage properties	$m^{\check{f}}$	$\phi^{\check{f}}$	$\phi_C^{\check{f}}$		
	10	0.70 MPa	0.55 MPa		
Compressive properties					
Mechanical properties	$E_L^{\check{f}}$	$E_T^{\check{f}}$	$\nu_L^{\check{f}}$	$\nu_T^{\check{f}}$	$G_L^{\check{f}}$
	22.04 MPa	22.04 MPa	0.25	0.25	8.82 MPa
Damage properties	$m^{\check{f}}$	$\phi^{\check{f}}$	$\phi_C^{\check{f}}$		
	10	5 MPa	1.2 MPa		
Soft region (Rubber matrix): Isotropic Mooney–Rivlin, Eq. (9)					
Tensile properties					
Mechanical Properties	$C_{10}^{\check{m}}$	$C_{01}^{\check{m}}$	$\kappa^{\check{m}}$		
	0.3 MPa	0.1 MPa	3.0		
Damage Properties	$m^{\check{m}}$	$\phi^{\check{m}}$	$\phi_C^{\check{m}}$		
	2	0.120 MPa	0.052 MPa		
Compressive properties					
Mechanical properties	$C_{10}^{\check{m}}$	$C_{01}^{\check{m}}$	$\kappa^{\check{m}}$		
	0.3 MPa	0.1 MPa	3.0		
Damage properties	$m^{\check{m}}$	$\phi^{\check{m}}$	$\phi_C^{\check{m}}$		
	2	0.30 MPa	0.07 MPa		

4.5 Effect of the interaction between neighboring fibers

In the previous examples, the microstructure contained repeating arrays of fibers with the exact same form of waviness. This results in uniform damage and failure patterns throughout the entire composite. In a more realistic case, the fibers within the composite will have slightly different waviness leading to a localization of the failure depending on the vicinity of the fibers to each other. In the present example, the analysis of a rubber matrix reinforced by nylon fibers is examined. The constitutive material models presently chosen for these composites are the isotropic SVK model for the nylon fibers (see Eq. (5)) and a hyperelastic compressible Mooney–Rivlin strain energy for the rubber matrix-media (see Eq. (9)). The mechanical elastic, damage, and failure properties of the nylon fibers and the rubber matrix are presented in Table 5 for the response in tension and compression states. The validity of the PHFGMC was verified with finite element analysis by Breiman et al. [50] for the elastic response of the considered composite.

Two arrangements of the fibers are presently considered for the architecture of the RUC, both with the geometrical dimensions of $u_{2f}^I/L = 5.0 \times 10^{-2}$, $H/d_f = 15$, and $d_f/L = 0.25$. The first RUC consists of two fibers with mirrored ('anti-phase') waviness shape, whereas in the second one, the fibers have identical ('in-phase') waviness shape as seen on the left-hand side of Fig. 11a, b, respectively. Subcell discretization in each of the RUCs was performed using the mesh generator described in Fig. 4 for each of the fibers (i.e., for the left and right halves of the RUC) to produce fine discretization at the fiber–matrix interface. It can be observed that in the former anti-phase arrangement of the fibers, there are areas in the RUC in which the fibers are closer to each other as compared to the composite with an in-phase waviness shape pattern. To illustrate this effect, consider a uniaxial tensile stress loading which is applied on the two types of the composites (i.e., $P_{33}^0 \neq 0$, and all other components are enforced to be zero). On the right-hand side of each Subfigure, the macroscale response of the composite $P_{33}^0 - F_{33}^0$ and the longitudinal tensile components $F_{33}^{(\beta)}$ and $P_{33}^{(\beta)}$ at point A, which indicates that $F_{33}^0 = 1.1$, are shown. By comparing the $F_{33}^{(\beta)}$ and $P_{33}^{(\beta)}$ distributions in the two arrangements presented in (a) and (b), it appears that the resulting maximum and minimum values are similar. However, the $F_{33}^{(\beta)}$ values in the in-phase architecture are far more localized, leading to a $\sim 50\%$ drop in the tensile strength of the composite compared to the predicted strength in the anti-phase fibers.

As to the initial failure envelopes of the considered composites, they were generated as previously described in Sect. 4.4, based on the tension–compression switch criterion of Eq. (50). For each applied biaxial stress state, the results are presented in terms of the stress and deformation gradient components. The predicted stress

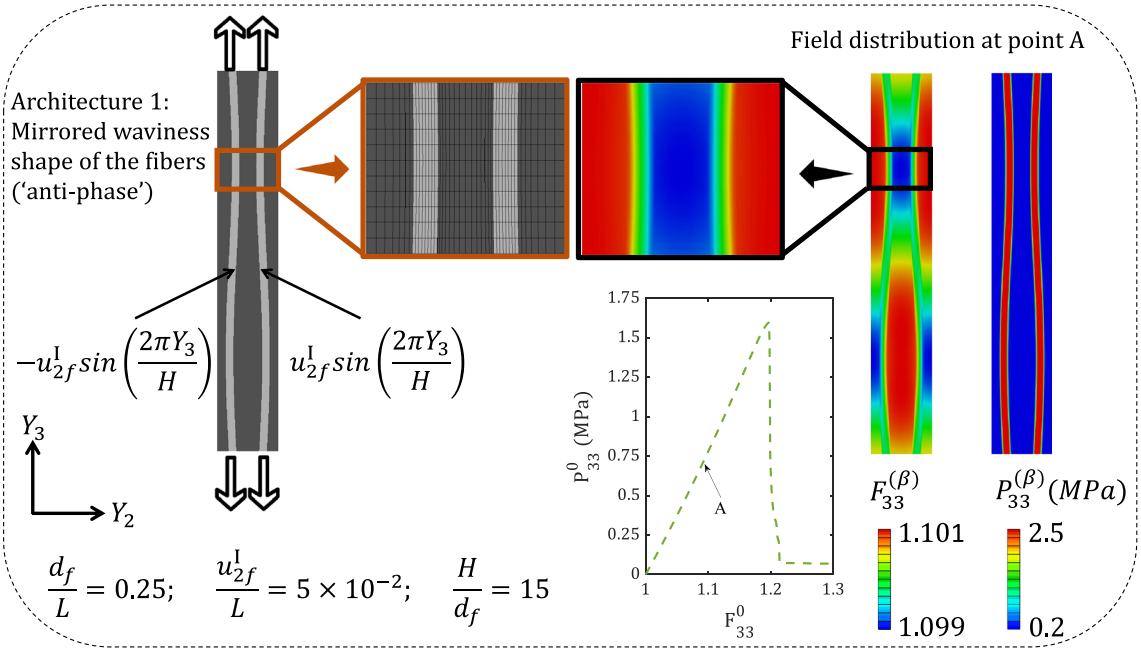

(a)

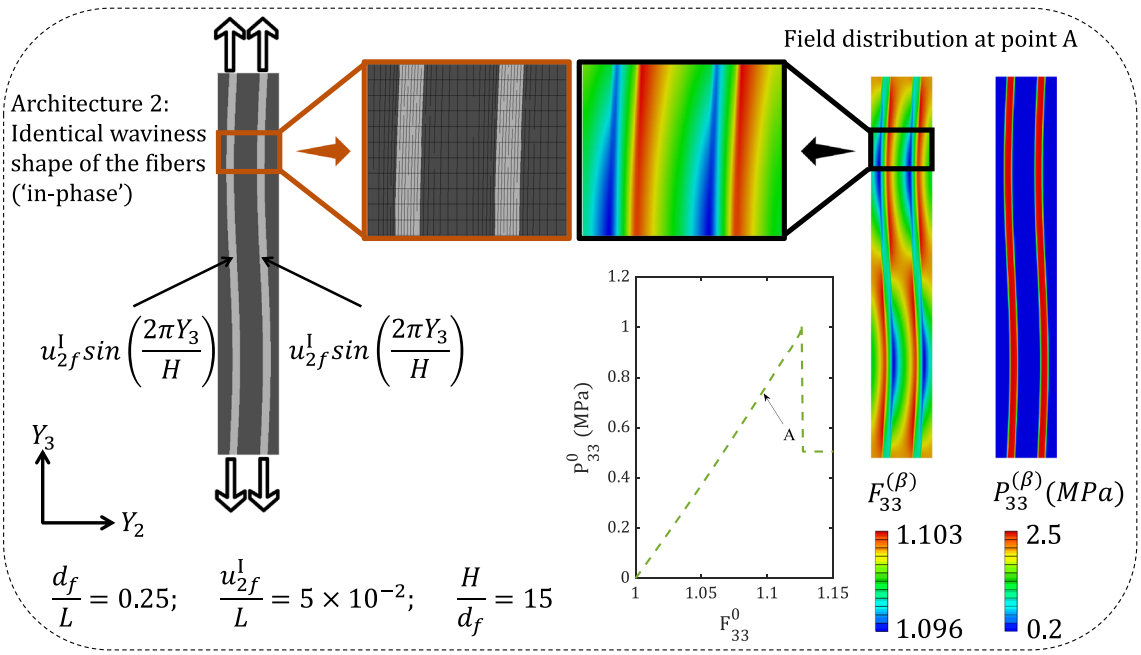

(b)

Fig. 11 PHFGMC results of wavy-layered composites subjected to longitudinal tensile stress. The anti-phase and in-phase architectures of the RUC are presented on the left-hand side of (**a**) and (**b**), respectively. The macroscale response of the composite and the microscale field distribution of the longitudinal components of the deformation gradient and the first Piola–Kirchhoff tensors are presented on the right-hand side of each Subfigure

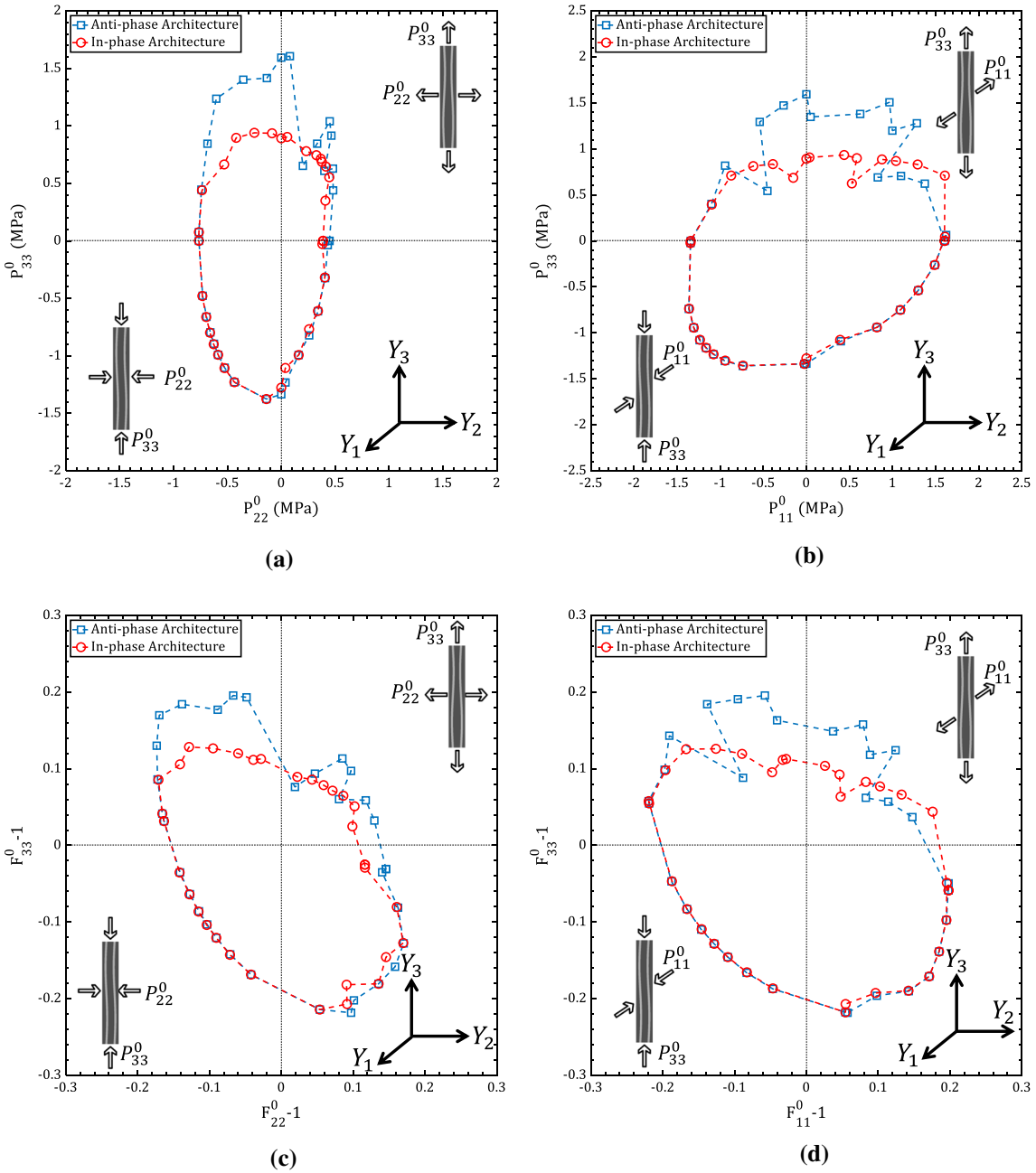

Fig. 12 PHFGMC initial failure envelopes prediction for a nylon/rubber composite system. The constituents' elastic, damage, and failure properties are given in Table 5

envelopes in the $P^0_{22} - P^0_{33}$ and $P^0_{11} - P^0_{33}$ planes are presented in Fig. 12a, b, respectively. The corresponding deformation gradient components at the initial failure, $F^0_{22} - F^0_{33}$ and $F^0_{11} - F^0_{33}$, were used to generate the analogous failure envelopes which are presented in Fig. 12c, d, respectively. It can be observed that the two architectures result in very similar initial stress and deformation gradient failure values when both of the applied stresses are in compression. However, in all other 3 quarters, there are significant differences between the two architectures. This reflects the previously discussed significant difference in tensile strength between the in-phase and anti-phase RUCs, as observed in Fig. 11. This highlights the effect of the waviness arrangement of the fibers on the microscale fluctuation values, which strongly influence the macroscale failure stresses and stretches.

5 Conclusions

In the present investigation, the finite strain PHFGMC was formulated for anisotropic constituents and further extended to account for damage at the microscale according to the energy limiters damage theory previously utilized for the HFGMC by Aboudi and Volokh [34]. In addition, an incremental-iterative scheme has been developed and applied for the prediction of progressive failure of composites in several mechanical load cases. This new ability has been applied on wavy-layered composites subjected to a uniaxial compressive stress state. It has been shown that there is a significant influence of the geometrical dimensions of the composite's microstructure and fiber waviness on the overall stiffness, strength, and failure mechanism.

Moreover, the results presented in this paper highlighted the important effect of the anisotropy of the constituents on the microscale and macroscale mechanical response. This was demonstrated by employing the proposed incremental-iterative PHFGMC scheme on two- and three-phased composites. For the latter case, the results pointed out that directed aligned anisotropy of the interphase layer could significantly influence the composite compressive behavior.

Additionally, the comparison between the responses of the high modulus carbon-based (HM-CFRP) and the boron-based (BFRP) composites exhibited the difference between the stress field distribution and the initial failure patterns at the microlevel. These differences are mainly caused by the significant contrast between the longitudinal shear and transverse moduli of the carbon and boron fibers.

As a practical application of the present theory, the PHFGMC was implemented on the commonly used carbon/epoxy system (IM7/977-3). This required an extensive calibration procedure with available tensile and compressive experimental data, performed in this study and taken from Clay and Knoth [45]. The proposed PHFGMC with damage allows for the calibrated elastic and failure parameters to differ in compression and tension states. This was especially pronounced in the analysis of this material system at biaxial stress state, as the use of a tension–compression criterion generated a more realistic and accurate failure envelope. The benefit of using this type of tension–compression switch was also demonstrated for the prediction of the mechanical elastic damage and failure of nylon-rubber composites. Specifically, the effect of the architecture of the microstructure (i.e., uniform or nonuniform waviness) was investigated for this system. The fiber waviness arrangement was found to have a significant role in the strength and the initial failure values of the nylon/rubber composite. In addition, significant localization differences were also observed when examining the deformation gradient components in the two considered architectures. Specifically, this leads to higher values near the fiber–matrix interface, which results in a premature failure at the microscale that effectively weakens the entire composite.

The proposed PHFGMC micromechanics can be further generalized to a triply periodic composite, where circular reinforcing fibers and particles can be considered. This will allow the investigation of damage and failure in these types of composites. Furthermore, this will enable to predict additional failure modes as buckling and debonding of the fibers and particles. In addition, the interaction between the fibers, waviness, and misalignment in more than one direction can be considered.

Finally, the present doubly periodic PHFGMC model can be utilized in a multiscale analysis, in conjunction with a finite element approach, to provide the response of composite structures. This generalization was previously employed for linear small strain problems (e.g., Massarwa et al. [51], [22], among others).

Acknowledgements The last author gratefully acknowledges the support of the Nathan Cummings Chair in Mechanics.

Declarations

Authors' contributions All authors contributed to the study conception and design. Material preparation, data collection, and analysis were performed by Uri Breiman. The first draft of the manuscript was written by Uri Breiman, and all authors commented on previous versions of the manuscript. All authors read and approved the final manuscript.

Funding This research was supported by the Israel Science Foundation (ISF) (Grant No. 2314/19). The authors acknowledge the support by the joint USA-Israel air vehicle technologies (AVT) program.

Availability of data and materials Not applicable.

Competing interests The authors have no relevant financial or non-financial interests to disclose. The authors declare that they have no conflict of interest.

Ethics approval Not applicable.

Consent to participate Not applicable.

Consent for publication Not applicable.

Code availability Not applicable.

Appendix A: Strain energy function derivatives

As discussed in Sect. 2, the derivatives of the strain energy W, and those of the Cauchy–Green deformation tensor **C**, generate the instantaneous stiffness and Piola–Kirchhoff stress tensors' components. In the scope of this paper, the SVK and the Mooney–Rivlin strain energies are used to represent the hyperelastic mechanical behavior of the materials. To that end, the SVK energy function's nonzero first- and second-order derivatives with respect to the invariants I_1, I_2, I_3 and the pseudo-invariants I_4, I_5 are:

$$\begin{aligned}
\frac{\partial W}{\partial I_1} &= \mu + \frac{1}{4}(\lambda + 2\mu)(I_1 - 3) + \zeta(I_4 - 1),\\
\frac{\partial W}{\partial I_2} &= -\frac{1}{2}\mu,\\
\frac{\partial W}{\partial I_4} &= 2\eta(I_4 - 1) + \varphi + \zeta(I_1 - 3),\\
\frac{\partial W}{\partial I_5} &= -\frac{1}{2}\varphi,
\end{aligned} \tag{A.1}$$

$$\begin{aligned}
\frac{\partial^2 W}{\partial I_1^2} &= \frac{\mu}{2} + \frac{\lambda}{4},\\
\frac{\partial^2 W}{\partial I_1 \partial I_4} &= \zeta,\\
\frac{\partial^2 W}{\partial I_4^2} &= 2\eta.
\end{aligned} \tag{A.2}$$

As for the Mooney–Rivlin energy function, the nonzero first- and second-order derivatives with respect to the invariants I_1, I_2, I_3 are

$$\begin{aligned}
\frac{\partial W}{\partial I_1} &= \frac{C_{10}}{I_3^{(1/3)}},\\
\frac{\partial W}{\partial I_2} &= \frac{C_{01}}{I_3^{(1/3)}},\\
\frac{\partial W}{\partial I_3} &= -\frac{C_{10} I_1}{3 I_3^{(4/3)}} - \frac{C_{01} I_2}{3 I_3^{(4/3)}} + \frac{\kappa(\sqrt{I_3} - 1)}{\sqrt{I_3}},
\end{aligned} \tag{A.3}$$

$$\frac{\partial^2 \mathrm{W}}{\partial \mathrm{I}_1 \partial \mathrm{I}_3} = -\frac{\mathrm{C}_{10}}{3\mathrm{I}_3^{(4/3)}},$$
$$\frac{\partial^2 \mathrm{W}}{\partial \mathrm{I}_2 \partial \mathrm{I}_3} = -\frac{\mathrm{C}_{01}}{3\mathrm{I}_3^{(4/3)}},$$
$$\frac{\partial^2 \mathrm{W}}{\partial \mathrm{I}_3^2} = \frac{4\mathrm{C}_{10}\mathrm{I}_1}{9\mathrm{I}_3^{(7/3)}} + \frac{4\mathrm{C}_{01}\mathrm{I}_2}{9\mathrm{I}_3^{(7/3)}} + \frac{\kappa}{2\mathrm{I}_3} - \frac{\kappa(\sqrt{\mathrm{I}_3} - 1)}{2\mathrm{I}_3^{(3/2)}}. \tag{A.4}$$

The first-order derivatives of the invariants and pseudo-invariants with respect to the right Cauchy–Green tensor's components C_{ij} are:

$$\frac{\partial \mathrm{I}_1}{\partial C_{ij}} = \delta_{ij},$$
$$\frac{\partial \mathrm{I}_2}{\partial C_{ij}} = \mathrm{I}_1\delta_{ij} - C_{ij},$$
$$\frac{\partial \mathrm{I}_3}{\partial C_{ij}} = \mathrm{I}_2\delta_{ij} - \mathrm{I}_1 C_{ij} + C_{ij}^2,$$
$$\frac{\partial \mathrm{I}_4}{\partial C_{ij}} = A_i A_j,$$
$$\frac{\partial \mathrm{I}_5}{\partial C_{ij}} = C_{jk}A_i A_k + C_{ik}A_k A_j, \tag{A.5}$$

and their second-order derivatives are:

$$\frac{\partial^2 \mathrm{I}_1}{\partial C_{ij}\partial C_{kl}} = 0,$$
$$\frac{\partial^2 \mathrm{I}_2}{\partial C_{ij}\partial C_{kl}} = \delta_{ij}\delta_{kl} - \frac{1}{2}(\delta_{ik}\delta_{jl} + \delta_{il}\delta_{jk}),$$
$$\frac{\partial^2 \mathrm{I}_3}{\partial C_{ij}\partial C_{kl}} = (\mathrm{I}_1\delta_{kl} - C_{kl})\delta_{ij} - \frac{1}{2}\mathrm{I}_1(\delta_{ik}\delta_{jl} + \delta_{il}\delta_{jk}) -$$
$$C_{ij}\delta_{kl} + \frac{1}{2}(\delta_{ik}C_{jl} + \delta_{il}C_{jk}) + \frac{1}{2}(\delta_{jl}C_{ik} + \delta_{jk}C_{il}),$$
$$\frac{\partial^2 \mathrm{I}_4}{\partial C_{ij}\partial C_{kl}} = 0,$$
$$\frac{\partial^2 \mathrm{I}_5}{\partial C_{ij}\partial C_{kl}} = \delta_{jk}A_i A_l + \delta_{il}A_j A_k. \tag{A.6}$$

Appendix B: Deformation gradient–microvariables coefficient matrix

The nonzero components of $\mathbf{A}_{\mathrm{w}}^{(\beta)}$ are (superscript β is omitted for clarity):

$$A_{w_{2,1}} = \left(\frac{1}{4}r_3\right)\check{J}_{22} + \left(-\frac{1}{2} + \frac{1}{4}r_2 + \frac{3}{2}r_3\right)\check{J}_{32},$$
$$A_{w_{2,4}} = \left(\frac{1}{2} + \frac{3}{2}r_2 + \frac{1}{4}r_3\right)\check{J}_{22} + \left(\frac{1}{4}r_2\right)\check{J}_{32},$$
$$A_{w_{2,7}} = \left(\frac{1}{4}r_3\right)\check{J}_{22} + \left(\frac{1}{2} + \frac{1}{4}r_2 + \frac{3}{2}r_3\right)\check{J}_{32},$$
$$A_{w_{2,10}} = \left(-\frac{1}{2} + \frac{3}{2}r_2 + \frac{1}{4}r_3\right)\check{J}_{22} + \left(\frac{1}{4}r_2\right)\check{J}_{32},$$

$$A_{w_{2,13}} = (-3r_2 - r_3)\,\check{J}_{22} + (-r_2 - 3r_3)\,\check{J}_{32}, \tag{B.1}$$

$$A_{w_{3,1}} = \left(\frac{1}{4}r_3\right)\check{J}_{23} + \left(-\frac{1}{2} + \frac{1}{4}r_2 + \frac{3}{2}r_3\right)\check{J}_{33},$$

$$A_{w_{3,4}} = \left(\frac{1}{2} + \frac{3}{2}r_2 + \frac{1}{4}r_3\right)\check{J}_{23} + \left(\frac{1}{4}r_2\right)\check{J}_{33},$$

$$A_{w_{3,7}} = \left(\frac{1}{4}r_3\right)\check{J}_{23} + \left(\frac{1}{2} + \frac{1}{4}r_2 + \frac{3}{2}r_3\right)\check{J}_{33},$$

$$A_{w_{3,10}} = \left(-\frac{1}{2} + \frac{3}{2}r_2 + \frac{1}{4}r_3\right)\check{J}_{23} + \left(\frac{1}{4}r_2\right)\check{J}_{33},$$

$$A_{w_{3,13}} = (-3r_2 - r_3)\,\check{J}_{23} + (-r_2 - 3r_3)\,\check{J}_{33}, \tag{B.2}$$

$$A_{w_{5,2}} = \left(\frac{1}{4}r_3\right)\check{J}_{22} + \left(-\frac{1}{2} + \frac{1}{4}r_2 + \frac{3}{2}r_3\right)\check{J}_{32},$$

$$A_{w_{5,5}} = \left(\frac{1}{2} + \frac{3}{2}r_2 + \frac{1}{4}r_3\right)\check{J}_{22} + \left(\frac{1}{4}r_2\right)\check{J}_{32},$$

$$A_{w_{5,8}} = \left(\frac{1}{4}r_3\right)\check{J}_{22} + \left(\frac{1}{2} + \frac{1}{4}r_2 + \frac{3}{2}r_3\right)\check{J}_{32},$$

$$A_{w_{5,11}} = \left(-\frac{1}{2} + \frac{3}{2}r_2 + \frac{1}{4}r_3\right)\check{J}_{22} + \left(\frac{1}{4}r_2\right)\check{J}_{32},$$

$$A_{w_{5,14}} = (-3r_2 - r_3)\,\check{J}_{22} + (-r_2 - 3r_3)\,\check{J}_{32}, \tag{B.3}$$

$$A_{w_{6,2}} = \left(\frac{1}{4}r_3\right)\check{J}_{23} + \left(-\frac{1}{2} + \frac{1}{4}r_2 + \frac{3}{2}r_3\right)\check{J}_{33},$$

$$A_{w_{6,5}} = \left(\frac{1}{2} + \frac{3}{2}r_2 + \frac{1}{4}r_3\right)\check{J}_{23} + \left(\frac{1}{4}r_2\right)\check{J}_{33},$$

$$A_{w_{6,8}} = \left(\frac{1}{4}r_3\right)\check{J}_{23} + \left(\frac{1}{2} + \frac{1}{4}r_2 + \frac{3}{2}r_3\right)\check{J}_{33},$$

$$A_{w_{6,11}} = \left(-\frac{1}{2} + \frac{3}{2}r_2 + \frac{1}{4}r_3\right)\check{J}_{23} + \left(\frac{1}{4}r_2\right)\check{J}_{33},$$

$$A_{w_{6,14}} = (-3r_2 - r_3)\,\check{J}_{23} + (-r_2 - 3r_3)\,\check{J}_{33}, \tag{B.4}$$

$$A_{w_{8,3}} = \left(\frac{1}{4}r_3\right)\check{J}_{22} + \left(-\frac{1}{2} + \frac{1}{4}r_2 + \frac{3}{2}r_3\right)\check{J}_{32},$$

$$A_{w_{8,6}} = \left(\frac{1}{2} + \frac{3}{2}r_2 + \frac{1}{4}r_3\right)\check{J}_{22} + \left(\frac{1}{4}r_2\right)\check{J}_{32},$$

$$A_{w_{8,9}} = \left(\frac{1}{4}r_3\right)\check{J}_{22} + \left(\frac{1}{2} + \frac{1}{4}r_2 + \frac{3}{2}r_3\right)\check{J}_{32},$$

$$A_{w_{8,12}} = \left(-\frac{1}{2} + \frac{3}{2}r_2 + \frac{1}{4}r_3\right)\check{J}_{22} + \left(\frac{1}{4}r_2\right)\check{J}_{32},$$

$$A_{w_{8,15}} = (-3r_2 - r_3)\,\check{J}_{22} + (-r_2 - 3r_3)\,\check{J}_{32}, \tag{B.5}$$

$$A_{w_{9,3}} = \left(\frac{1}{4}r_3\right)\check{J}_{23} + \left(-\frac{1}{2} + \frac{1}{4}r_2 + \frac{3}{2}r_3\right)\check{J}_{33},$$

$$A_{w_{9,6}} = \left(\frac{1}{2} + \frac{3}{2}r_2 + \frac{1}{4}r_3\right)\check{J}_{23} + \left(\frac{1}{4}r_2\right)\check{J}_{33},$$

$$A_{w_{9,9}} = \left(\frac{1}{4}r_3\right)\check{J}_{23} + \left(\frac{1}{2} + \frac{1}{4}r_2 + \frac{3}{2}r_3\right)\check{J}_{33},$$

$$A_{w_{9,12}} = \left(-\frac{1}{2} + \frac{3}{2}r_2 + \frac{1}{4}r_3\right)\check{J}_{23} + \left(\frac{1}{4}r_2\right)\check{J}_{33},$$
$$A_{w_{9,15}} = (-3r_2 - r_3)\,\check{J}_{23} + (-r_2 - 3r_3)\,\check{J}_{33} \tag{B.6}$$

where $\check{J}_{ij}$ are the components of the Jacobeian matrix of the inverse mapping as defined in Eq. (21).

Appendix C: Creation of the overall set of equations

As pointed out in Sect. 3, the equilibrium of the entire composite must be assured during loading. This is governed by the PHFGMC equations as follows. Firstly, since the micromechanical analysis of the composite is at both the micro- and macroscales, the equilibrium is achieved in a two-scale manner. To that end, the internal resisting vectors are balanced by the homogenized-field force vector, $\mathbf{Q}_{\mathrm{F}^0}$, and the fluctuation-field force vector, $\mathbf{Q}_{\mathrm{w}}$, by

$$\left\{\begin{array}{c}\mathbf{Q}_{\mathrm{F}^0}\\ \mathbf{Q}_{\mathrm{w}}\end{array}\right\} - \left\{\begin{array}{c}\mathbf{I}_{\mathrm{F}^0}\\ \mathbf{I}_{\mathrm{w}}\end{array}\right\} = \left\{\begin{array}{c}\mathbf{0}\\ \mathbf{0}\end{array}\right\}. \tag{C.1}$$

Secondly, satisfying Eq. (C.1) for a nonlinear analysis is challenging to achieve in an exact manner. Therefore, a numerical routine must be employed, in which a residual vector $\mathbf{R}^{es}$ is defined to fulfill the equilibrium conditions in an approximate manner as

$$\left\{\begin{array}{c}\mathbf{R}^{es}_{\mathrm{F}^0}\\ \mathbf{R}^{es}_{\mathrm{w}}\end{array}\right\} \equiv \left\{\begin{array}{c}\mathbf{Q}_{\mathrm{F}^0}\\ \mathbf{Q}_{\mathrm{w}}\end{array}\right\} - \left\{\begin{array}{c}\mathbf{I}_{\mathrm{F}^0}\\ \mathbf{I}_{\mathrm{w}}\end{array}\right\} \approx \left\{\begin{array}{c}\mathbf{0}\\ \mathbf{0}\end{array}\right\}. \tag{C.2}$$

Furthermore, in incremental-scheme solutions, it is possible to use the first-order terms of the Taylor expansion in order to linearize the set of micromechanical equations. For a general increment, q, the residual will be evaluated as

$$\mathbf{R}^{es}\big|_{(\mathbf{w}_{\mathrm{q}},\mathbf{F}^0_{\mathrm{q}})} \approx \mathbf{R}^{es}\big|_{(\mathbf{w}_{\mathrm{q-1}},\mathbf{F}^0_{\mathrm{q-1}})} + \left.\frac{\partial \mathbf{R}^{es}}{\partial \mathbf{w}}\right|_{(\mathbf{w}_{\mathrm{q-1}},\mathbf{F}^0_{\mathrm{q-1}})} \Delta\mathbf{w}_{\mathrm{q}} + \left.\frac{\partial \mathbf{R}^{es}}{\partial \mathbf{F}^0}\right|_{(\mathbf{w}_{\mathrm{q-1}},\mathbf{F}^0_{\mathrm{q-1}})} \Delta\mathbf{F}^0_{\mathrm{q}}. \tag{C.3}$$

In addition, it should be noted that in the framework of the proposed PHFGMC, there are no applied forces associated with the microvariables. Therefore, the residual at the previous increment $(q-1)$ is reduced to

$$\mathbf{R}^{es}_{\mathrm{w}}\big|_{(\mathbf{w}_{\mathrm{q-1}},\mathbf{F}^0_{\mathrm{q-1}})} = \mathbf{Q}_{\mathrm{w}_{\mathrm{q-1}}} - \mathbf{I}_{\mathrm{w}_{\mathrm{q-1}}} = -\mathbf{I}_{\mathrm{w}_{\mathrm{q-1}}},$$
$$\mathbf{R}^{es}_{\mathrm{F}^0}\big|_{(\mathbf{w}_{\mathrm{q-1}},\mathbf{F}^0_{\mathrm{q-1}})} = \mathbf{Q}_{\mathrm{F}^0{}_{\mathrm{q-1}}} - \mathbf{I}_{\mathrm{F}^0{}_{\mathrm{q-1}}}. \tag{C.4}$$

Hence, the partial derivatives of $\mathbf{R}^{es}$ from Eq. (C.3) are given by

$$\begin{aligned}
\frac{\partial \mathbf{R}^{es}_{\mathrm{w}}}{\partial \mathbf{w}} &= \frac{\partial \mathbf{Q}_{\mathrm{w}}}{\partial \mathbf{w}} - \frac{\partial \mathbf{I}_{\mathrm{w}}}{\partial \mathbf{w}} = -\frac{\partial \mathbf{I}_{\mathrm{w}}}{\partial \mathbf{w}},\\
\frac{\partial \mathbf{R}^{es}_{\mathrm{F}^0}}{\partial \mathbf{w}} &= \frac{\partial \mathbf{Q}_{\mathrm{F}^0}}{\partial \mathbf{w}} - \frac{\partial \mathbf{I}_{\mathrm{F}^0}}{\partial \mathbf{w}} = -\frac{\partial \mathbf{I}_{\mathrm{F}^0}}{\partial \mathbf{w}},\\
\frac{\partial \mathbf{R}^{es}_{\mathrm{w}}}{\partial \mathbf{F}^0} &= \frac{\partial \mathbf{Q}_{\mathrm{w}}}{\partial \mathbf{F}^0} - \frac{\partial \mathbf{I}_{\mathrm{w}}}{\partial \mathbf{F}^0} = -\frac{\partial \mathbf{I}_{\mathrm{w}}}{\partial \mathbf{F}^0},\\
\frac{\partial \mathbf{R}^{es}_{\mathrm{F}^0}}{\partial \mathbf{F}^0} &= \frac{\partial \mathbf{Q}_{\mathrm{F}^0}}{\partial \mathbf{F}^0} - \frac{\partial \mathbf{I}_{\mathrm{F}^0}}{\partial \mathbf{F}^0} = -\frac{\partial \mathbf{I}_{\mathrm{F}^0}}{\partial \mathbf{F}^0},
\end{aligned} \tag{C.5}$$

and the partial derivatives of the internal resisting vectors, which are given in Eqs. (34–35), are

$$\begin{aligned}
\frac{\partial \mathbf{I}_{\mathrm{w}}}{\partial \mathbf{w}} &= \frac{\partial}{\partial \mathbf{w}}\int_V \mathbf{A}_{\mathrm{w}}^{\mathrm{T}}\mathbf{P}\mathrm{d}V = \frac{\partial}{\partial \mathbf{w}}\int_V \mathbf{A}_{\mathrm{w}}^{\mathrm{T}}\mathbf{R}\mathbf{F}\mathrm{d}V\\
&= \frac{\partial}{\partial \mathbf{w}}\int_V \mathbf{A}_{\mathrm{w}}^{\mathrm{T}}\mathbf{R}(\mathbf{F}^0 + \mathbf{A}_{\mathrm{w}}\mathbf{w})\mathrm{d}V = \int_V \mathbf{A}_{\mathrm{w}}^{\mathrm{T}}\mathbf{R}\mathbf{A}_{\mathrm{w}}\mathrm{d}V \equiv \mathbf{K}_{\mathrm{ww}},
\end{aligned}$$

$$\begin{aligned}
\frac{\partial \mathbf{I}_{\mathrm{F}^0}}{\partial \mathbf{w}} &= \frac{\partial}{\partial \mathbf{w}} \int_V \mathbf{P} \mathrm{d}V = \frac{\partial}{\partial \mathbf{w}} \int_V \mathbf{R}\mathbf{F} \mathrm{d}V \\
&= \frac{\partial}{\partial \mathbf{w}} \int_V \mathbf{R}(\mathbf{F}^0 + \mathbf{A}_{\mathrm{w}}\mathbf{w}) \mathrm{d}V = \int_V \mathbf{R}\mathbf{A}_{\mathrm{w}} \mathrm{d}V \equiv \mathbf{K}_{\mathrm{F}^0\mathrm{w}}, \\
\frac{\partial \mathbf{I}_{\mathrm{w}}}{\partial \mathbf{F}^0} &= \frac{\partial}{\partial \mathbf{F}^0} \int_V \mathbf{A}_{\mathrm{w}}^{\mathrm{T}} \mathbf{P} \mathrm{d}V = \frac{\partial}{\partial \mathbf{w}} \int_V \mathbf{A}_{\mathrm{w}}^{\mathrm{T}} \mathbf{R}\mathbf{F} \mathrm{d}V \\
&= \frac{\partial}{\partial \mathbf{F}^0} \int_V \mathbf{A}_{\mathrm{w}}^{\mathrm{T}} \mathbf{R}(\mathbf{F}^0 + \mathbf{A}_{\mathrm{w}}\mathbf{w}) \mathrm{d}V = \int_V \mathbf{A}_{\mathrm{w}}^{\mathrm{T}} \mathbf{R} \mathrm{d}V \equiv \mathbf{K}_{\mathrm{w}\mathrm{F}^0}, \\
\frac{\partial \mathbf{I}_{\mathrm{F}^0}}{\partial \mathbf{F}^0} &= \frac{\partial}{\partial \mathbf{F}^0} \int_V \mathbf{P} \mathrm{d}V = \frac{\partial}{\partial \mathbf{F}^0} \int_V \mathbf{R}\mathbf{F} \mathrm{d}V \\
&= \frac{\partial}{\partial \mathbf{w}} \int_V \mathbf{R}(\mathbf{F}^0 + \mathbf{A}_{\mathrm{w}}\mathbf{w}) \mathrm{d}V = \int_V \mathbf{R} \mathrm{d}V \equiv \mathbf{K}_{\mathrm{F}^0\mathrm{F}^0}.
\end{aligned} \tag{C.6}$$

Finally, using Eqs. (C.3–C.6), the linearized-incremental PHFGMC equations are given in a 'matrix-form' as

$$\begin{bmatrix} \mathbf{K}_{\mathrm{ww}} & \mathbf{K}_{\mathrm{w}\mathrm{F}^0} \\ \mathbf{K}_{\mathrm{F}^0\mathrm{w}} & \mathbf{K}_{\mathrm{F}^0\mathrm{F}^0} \end{bmatrix} \begin{Bmatrix} \Delta \mathbf{w} \\ \Delta \mathbf{F}^0 \end{Bmatrix} = \begin{Bmatrix} -\mathbf{I}_{\mathrm{w}} \\ \mathbf{Q}_{\mathrm{F}^0} - \mathbf{I}_{\mathrm{F}^0} \end{Bmatrix}. \tag{C.7}$$

In the present investigation, the composite's incremental deformation gradient $\Delta \mathbf{F}^{\mathbf{0}}$ is known at each increment, thus the matrix-form presented in Eq. (C.7) is reduced to

$$\mathbf{K}_{\mathrm{ww}} \Delta \mathbf{w} = -\mathbf{I}_{\mathrm{w}} - \mathbf{K}_{\mathrm{w}\mathrm{F}^0} \Delta \mathbf{F}^0 \tag{C.8}$$

in which the 'stiffness matrices' $\mathbf{K}_{\mathrm{ww}}$ and $\mathbf{K}_{\mathrm{w}\mathrm{F}^0}$ are calculated according to an assembly procedure, and the subcell's 'stiffness matrices' are defined explicitly as

$$\begin{aligned}
\mathbf{K}_{\mathrm{ww}}^{(\beta)} &= \int_{V^{(\beta)}} \mathbf{A}_{\mathrm{w}}^{(\beta),\mathrm{T}} \mathbf{R}^{(\beta)} \mathbf{A}_{\mathrm{w}}^{(\beta)} \mathrm{d}V, \\
\mathbf{K}_{\mathrm{w}\mathrm{F}^0}^{(\beta)} &= \int_{V^{(\beta)}} \mathbf{A}_{\mathrm{w}}^{(\beta),\mathrm{T}} \mathbf{R}^{(\beta)} \mathrm{d}V, \\
\mathbf{K}_{\mathrm{F}^0\mathrm{w}}^{(\beta)} &= \int_{V^{(\beta)}} \mathbf{R}^{(\beta)} \mathbf{A}_{\mathrm{w}}^{(\beta)} \mathrm{d}V, \\
\mathbf{K}_{\mathrm{F}^0\mathrm{F}^0}^{(\beta)} &= \int_{V^{(\beta)}} \mathbf{R}^{(\beta)} \mathrm{d}V.
\end{aligned} \tag{C.9}$$

Appendix D: Calibration of IM7/977-3 elastic and failure properties

The elastic and failure properties of the IM7 fiber and 977-3 matrix materials are determined by a lengthy calibration scheme. This procedure is necessary in order to generate the effective response (i.e., instantaneous stiffness and strength) of the composite at uniaxial and biaxial loading, as discussed in Sect. 4.4. This Appendix will present the details on the calibration of the properties to experimental results of the laminate and its constituents, and additional published data. The finalized properties are presented in Table 4.

According to the elastic and strength results provided from the manufacturer tensile experiments of these Hexcel® IM7 fibers [52], the longitudinal elastic modulus of the fiber, $E_L^{\check{f}}$, was determined to be 276 GPa, and the failure properties were set to be $m^{\check{f}} = 10.0$, $\phi^{\check{f}} = 80$ MPa, and $\phi_C^{\check{f}} = 60$ MPa. Additional fiber elastic properties used for this composite system were adopted from the fitted values determined by Massarwa et al. [51] as $E_T^{\check{f}}$=16 GPa, $\nu_L^{\check{f}}$=0.31, $\nu_T^{\check{f}}$=0.28, and $G_L^{\check{f}}$=15 GPa. The elastic properties of the epoxy resin 977-3 of Solvay® [53] were assigned as $E_L^{\check{m}} = E_T^{\check{m}} = 3.7$ GPa and $\nu_L^{\check{m}} = \nu_T^{\check{m}} = 0.37$, corresponding to those calibrated by Bogdanor and Oskay [46]. For the failure properties of the epoxy, the calibration was performed to capture the reported tensile strength of 82 MPa [54], which derived the values of $m^{\check{m}} = 2.0$, $\phi^{\check{m}} = 2.8$ MPa, and $\phi_C^{\check{m}} = 1.3$ MPa.

The composite is modeled by a layered RUC and constructed out of only fiber and matrix phases (without voids), with a 65% fiber volume fraction, which is similar to the average value reported by Clay and Knoth [45]. The geometrical dimensions of the wavy-layered RUC, $u_2^I/L = 2.5 \times 10^{-2}$ and $H/d_f = 15$, were determined by using the 0° UD tensile experimental results which were performed by Clay and Knoth [45]. The results of the 90° UD tensile experiments, as well as the 90° bending experiments, suggested to re-calibrate $E_T^{\check{f}}$ to 13 GPa. Using this value, which is similar to the calibrated value reported by Bogdanor and Oskay [46], the effective stiffness of the composite coincides with the transverse experimental response. In terms of strength, it was indicated by Clay and Knoth [45] that some issues in the 90° UD tensile experiments caused premature brittle failure at unacceptable failure location. This experimental challenges outcome in a very low transverse strength with respect to similar CFRPs as mentioned by Dalgarno et al. [55] and by Bogdanor and Oskay [46]. Therefore, it has been chosen to keep the value of $E_T^{\check{f}}$ as 13 GPa, which provides a transverse strength value in the range of the reported transverse tensile and bending strengths in [45].

As indicated by Naghipour et al. [56], Bogdanor and Oskay [46], among others, the longitudinal compressive modulus of the fiber must be lower than its tensile stiffness in order to capture the effective stiffness of the composite under uniaxial compression loading. Therefore, for a compressive state of the fiber, the modulus is reduced to $E_L^{\check{f}}$=225 GPa, which is similar to the 215 GPa calibrated previously by Naghipour et al. [56] and by Bogdanor and Oskay [46]. In addition, there is a significant difference in the general trend of the stress–strain relation between a linear response for the 0° UD tensile experiments to the nonlinear response observed in the 0° UD compressive experiments. To that end, a new set of energy parameters, $m^{\check{f}} = 1.0$, $\phi^{\check{f}} = 120$ MPa, and $\phi_C^{\check{f}} = 18$ MPa, has been determined to capture the compressive response of the composite best.

Unlike the fiber, the elastic response of the matrix is similar at tension and compression states. However, for typical epoxies, these mechanical behaviors coincide (in absolute values) only until the initiation of cracks at tension, which forms stress concentration and weakens the material. Thus, it requires to re-calibrate the matrix failure properties at compression according to the 90° UD compressive experiments, where the matrix is fully compressed. The final compressive fitted energy parameters for the matrix are $m^{\check{m}} = 2.0$, $\phi^{\check{m}} = 18$ MPa, and $\phi_C^{\check{m}} = 6$ MPa.

References

1. Kaddour, A.-S., Hinton, M.J.: Maturity of 3D failure criteria for fibre-reinforced composites: comparison between theories and experiments: Part B of WWFE-II. J. Compos. Mater. **47**(6–7), 925–966 (2013). https://doi.org/10.1177/0021998313478710
2. Kaddour, A., Hinton, M.: Benchmarking of triaxial failure criteria for composite laminates: comparison between models of 'Part (A)' of 'WWFE-II'. J. Compos. Mater. **46**(19–20), 2595–2634 (2012). https://doi.org/10.1177/0021998312449887
3. Kaddour, A., Hinton, M., Smith, P., Li, S.: A comparison between the predictive capability of matrix cracking, damage and failure criteria for fibre reinforced composite laminates: Part A of the third world-wide failure exercise. J. Compos. Mater. **47**(20–21), 2749–2779 (2013). https://doi.org/10.1177/0021998313499476
4. Engelstad, S.P., Clay, S.B.: Comparison of composite damage growth tools for static behavior of notched composite laminates. J. Compos. Mater. **51**(10), 1493–1524 (2017). https://doi.org/10.1177/0021998316675945
5. Daum, B., Feld, N., Allix, O., Rolfes, R.: A review of computational modelling approaches to compressive failure in laminates. Compos. Sci. Technol. **181**, 107663 (2019). https://doi.org/10.1016/j.compscitech.2019.05.020
6. Orifici, A.C., Herszberg, I., Thomson, R.S.: Review of methodologies for composite material modelling incorporating failure. Compos. Struct. **86**(1–3), 194–210 (2008). https://doi.org/10.1016/j.compstruct.2008.03.007
7. Li, W.: Damage models for soft tissues: a survey. J. Med. Biol. Eng. **36**(3), 285–307 (2016). https://doi.org/10.1007/s40846-016-0132-1
8. Voyiadjis, G.Z., Kattan, P.I.: Damage Mechanics. Tylor and Francis (CRC Press), New York (2005)
9. Aboudi, J., Arnold, S.M., Bednarcyk, B.A.: Practical Micromechanics of Composite Materials. Elsevier, USA (2021)
10. Jha, N.K., Reinoso, J., Dehghani, H., Merodio, J.: A computational model for fiber-reinforced composites: hyperelastic constitutive formulation including residual stresses and damage. Comput. Mech. (2018). https://doi.org/10.1007/s00466-018-1630-5
11. Nolan, D.R., Gower, A.L., Destrade, M., Ogden, R.W., McGarry, J.P.: A robust anisotropic hyperelastic formulation for the modelling of soft tissue. J. Mech. Behav. Biomed. Mater. **39**, 48–60 (2014). https://doi.org/10.1016/j.jmbbm.2014.06.016
12. Garcia-Gonzalez, D., Jérusalem, A., Garzon-Hernandez, S., Zaera, R., Arias, A.: A continuum mechanics constitutive framework for transverse isotropic soft tissues. J. Mech. Phys. Solids **112**, 209–224 (2018). https://doi.org/10.1016/j.jmps.2017.12.001
13. Holzapfel, G.A., Ogden, R.W., Sherifova, S.: On fibre dispersion modelling of soft biological tissues: a review. Proc. R. Soc. A **475**(2224), 20180736 (2019). https://doi.org/10.1098/rspa.2018.0736
14. Peña, J.A., Corral, V., Martinez, M.A., Pena, E.: Over length quantification of the multiaxial mechanical properties of the ascending, descending and abdominal aorta using digital image correlation. J. Mech. Behav. Biomed. Mater. **77**, 434–445 (2018). https://doi.org/10.1016/j.jmbbm.2017.10.007

15. Peña, J.A., Martínez, M.A., Peña, E.: Failure damage mechanical properties of thoracic and abdominal porcine aorta layers and related constitutive modeling: phenomenological and microstructural approach. Biomech. Model. Mechanobiol., 1–22 (2019). https://doi.org/10.1007/s10237-019-01170-0
16. Zeinali-Davarani, S., Wang, Y., Chow, M.-J., Turcotte, R., Zhang, Y.: Contribution of collagen fiber undulation to regional biomechanical properties along porcine thoracic aorta. J. Biomech. Eng. **137**(5), 051001 (2015). https://doi.org/10.1115/1.4029637
17. Aboudi, J., Arnold, S.M., Bednarcyk, B.A.: Micromechanics of Composite Materials: A Generalized Multiscale Approach. Elsevier, New York (2013)
18. Haj-Ali, R., Aboudi, J.: A new and general formulation of the parametric HFGMC micromechanical method for two and three-dimensional multi-phase composites. Int. J. Solids Struct. **50**(6), 907–919 (2013). https://doi.org/10.1016/j.ijsolstr.2012.11.009
19. Haj-Ali, R., Aboudi, J.: The parametric HFGMC micromechanics. In: Micromechanics and Nanomechanics of Composite Solids. Springer, Cham, pp. 391–424 (2018)
20. Levi-Sasson, A., Aboudi, J., Matzenmiller, A., Haj-Ali, R.: Failure envelopes for laminated composites by the parametric hfgmc micromechanical framework. Compos. Struct. **140**, 378–389 (2016). https://doi.org/10.1016/j.compstruct.2015.12.035
21. Massarwa, E., Aboudi, J., Galbusera, F., Wilke, H.-J., Haj-Ali, R.: A nonlinear micromechanical model for progressive damage of vertebral trabecular bones. J. Mech. Mater. Struct. **12**(4), 407–424 (2017). https://doi.org/10.2140/jomms.2017.12.407
22. Massarwa, E., Aboudi, J., Haj-Ali, R.: A multiscale modeling for failure predictions of fiber reinforced composite laminates. Compos. B Eng. **175**, 107166 (2019). https://doi.org/10.1016/j.compositesb.2019.107166
23. Meshi, I., Breiman, U., Aboudi, J., Haj-Ali, R.: The cohesive parametric high-fidelity-generalized-method-of-cells micromechanical model. Int. J. Solids Struct. **206**, 183–197 (2020). https://doi.org/10.1016/j.ijsolstr.2020.08.024
24. Breiman, U., Meshi, I., Aboudi, J., Haj-Ali, R.: Finite strain parametric HFGMC micromechanics of soft tissues. Biomech. Model. Mechanobiol. **19**, 2443–2453 (2020). https://doi.org/10.1007/s10237-020-01348-x
25. Korenczuk, C.E., Votava, L.E., Dhume, R.Y., Kizilski, S.B., Brown, G.E., Narain, R., Barocas, V.H.: Isotropic failure criteria are not appropriate for anisotropic fibrous biological tissues. J. Biomech. Eng. **139**(7) (2017). https://doi.org/10.1115/1.4036316
26. Liu, M., Dong, H., Lou, X., Iannucci, G., Chen, E.P., Leshnower, B.G., Sun, W.: A novel anisotropic failure criterion with dispersed fiber orientations for aortic tissues. J. Biomech. Eng. **142**(11) (2020). https://doi.org/10.1115/1.4048029
27. Maiti, S., Thunes, J.R., Fortunato, R.N., Gleason, T.G., Vorp, D.A.: Computational modeling of the strength of the ascending thoracic aortic media tissue under physiologic biaxial loading conditions. J. Biomech. **108**, 109884 (2020). https://doi.org/10.1016/j.jbiomech.2020.109884
28. Russ, J., Slesarenko, V., Rudykh, S., Waisman, H.: Rupture of 3d-printed hyperelastic composites: experiments and phase field fracture modeling. J. Mech. Phys. Solids **140**, 103941 (2020). https://doi.org/10.1016/j.jmps.2020.103941
29. Aboudi, J.: Finite strain micromechanical analysis of rubber-like matrix composites incorporating the Mullins damage effect. Int. J. Damage Mech **18**(1), 5–29 (2009). https://doi.org/10.1177/1056789507081845
30. Neto, E.D.S., Perić, D., Owen, D.: A phenomenological three-dimensional rate-idependent continuum damage model for highly filled polymers: formulation and computational aspects. J. Mech. Phys. Solids **42**(10), 1533–1550 (1994). https://doi.org/10.1016/0022-5096(94)90086-8
31. Volokh, K.Y.: Hyperelasticity with softening for modeling materials failure. J. Mech. Phys. Solids **55**(10), 2237–2264 (2007). https://doi.org/10.1016/j.jmps.2007.02.012
32. Volokh, K.: On modeling failure of rubber-like materials. Mech. Res. Commun. **37**(8), 684–689 (2010). https://doi.org/10.1016/j.mechrescom.2010.10.006
33. Volokh, K.Y.: Review of the energy limiters approach to modeling failure of rubber. Rubber Chem. Technol. **86**(3), 470–487 (2013). https://doi.org/10.5254/rct.13.87948
34. Aboudi, J., Volokh, K.Y.: Failure prediction of unidirectional composites undergoing large deformations. J. Appl. Mech. **82**(7), 71004 (2015). https://doi.org/10.1115/1.4030351
35. Aboudi, J., Volokh, K.Y.: Modeling deformation and failure of viscoelastic composites at finite strains. Mech. Soft Mater. **2**(1), 1–19 (2020). https://doi.org/10.1007/s42558-020-00028-1
36. Volokh, K.Y., Aboudi, J.: Aneurysm strength can decrease under calcification. J. Mech. Behav. Biomed. Mater. **57**, 164–174 (2016). https://doi.org/10.1016/j.jmbbm.2015.11.012
37. Holzapfel, G.A.: Nonlinear Solid Mechanics: a Continuum Approach for Engineering Science. Wiley, Chichester (2000)
38. Bonet, J., Burton, A.: A simple orthotropic, transversely isotropic hyperelastic constitutive equation for large strain computations. Comput. Methods Appl. Mech. Eng. **162**(1–4), 151–164 (1998). https://doi.org/10.1016/S0045-7825(97)00339-3
39. Sussman, T., Bathe, K.J.: A finite element formulation for nonlinear incompressible elastic and inelastic analysis. Comput. Struct. **26**(1), 357–409 (1987). https://doi.org/10.1016/0045-7949(87)90265-3
40. Schenk, O., Gärtner, K.: Solving unsymmetric sparse systems of linear equations with pardiso. Future Gener. Comput. Syst. **20**(3), 475–487 (2004). https://doi.org/10.1016/j.future.2003.07.011. (**Selected numerical algorithms**)
41. Intel®: Intel® oneAPI Math Kernel Library - Developer Reference (2022). Intel®. https://www.intel.com/content/www/us/en/develop/documentation/onemkl-developer-reference-fortran
42. Hughes, T.J.: Isoparametric elements and elementary programming concepts. In: The Finite Element Method: Linear Static and Dynamic Finite Element Analysis. Dover, New York, pp. 109–184 (2014)
43. Kim, Y.A., Hayashi, T., Endo, M., Gotoh, Y., Wada, N., Seiyama, J.: Fabrication of aligned carbon nanotube-filled rubber composite. Scripta Mater. **54**(1), 31–35 (2006). https://doi.org/10.1016/j.scriptamat.2005.09.014
44. Shi, D., He, P., Lian, J., Chaud, X., Bud'ko, S.L., Beaugnon, E., Wang, L., Ewing, R.C., Tournier, R.: Magnetic alignment of carbon nanofibers in polymer composites and anisotropy of mechanical properties. J. Appl. Phys. **97**(6), 064312 (2005). https://doi.org/10.1063/1.1861143

45. Clay, S.B., Knoth, P.M.: Experimental results of quasi-static testing for calibration and validation of composite progressive damage analysis methods. J. Compos. Mater. **51**(10), 1333–1353 (2017). https://doi.org/10.1177/0021998316658539
46. Bogdanor, M.J., Oskay, C.: Prediction of progressive damage and strength of IM7/977-3 composites using the eigendeformation-based homogenization approach: Static loading. J. Compos. Mater. **51**(10), 1455–1472 (2017). https://doi.org/10.1177/0021998316650982
47. Godines, C., DorMohammadi, S., Abdi, F., Montero, M.V., Huang, D., Minnetyan, L.: Damage tolerant composite design principles for aircraft components under static service loading using multi-scale progressive failure analysis. J. Compos. Mater. **51**(10), 1393–1419 (2017). https://doi.org/10.1177/0021998316671575
48. Holzapfel, G.A., Ogden, R.W.: On the tension-compression switch in soft fibrous solids. Eur. J. Mech.-A/Solids **49**, 561–569 (2015). https://doi.org/10.1016/j.euromechsol.2014.09.005
49. Dassault Systems, SIMULIA: Abaqus CAE Documentation, Anisotropic Hyperelastic Behavior (2021). Dassault Systems, SIMULIA. https://help.3ds.com/2021
50. Breiman, U., Meshi, I., Aboudi, J., Haj-Ali, R.: Finite strain parametric HFGMC prediction of the micromechanical behavior of composite. In: Proceeding of ICCM22. Engineers Australia, Melbourne, VIC, , pp. 4619–4624 (2019). https://search.informit.org/doi/10.3316/informit.888015848574221
51. Massarwa, E., Aboudi, J., Haj-Ali, R.: A multiscale progressive damage analysis for laminated composite structures using the parametric HFGMC micromechanics. Compos. Struct. **188**, 159–172 (2018). https://doi.org/10.1016/j.compstruct.2017.11.089
52. Hexcel®: HexTow® IM7 Carbon Fiber Product Data. (2020). Hexcel®. https://www.hexcel.com/Resources/DataSheets/Carbon-Fiber
53. Solvay®: Technical Data Sheet CYCOM® 977-3 Epoxy Resin (2017). Solvay®. https://www.solvay.com/en/product/cycom-977-3
54. Eberle, C.C., Janke, C.L., Sands, J.A., Wilenski, M.S.: Interfacial properties of electron beam cured composites. Technical Report ORNL-27 (4-00), Oak Ridge National Laboratory (2005). https://www.osti.gov/biblio/885946
55. Dalgarno, R.W., Action, J.E., Robbins, D.H., Engelstad, S.P.: Failure simulations of open-hole and unnotched IM7/977-3 coupons subjected to quasi-static loading using Autodesk Helius PFA. J. Compos. Mater. **51**(10), 1421–1432 (2017). https://doi.org/10.1177/0021998316653174
56. Naghipour, P., Arnold, S.M., Pineda, E.J., Stier, B., Hansen, L., Bednarcyk, B.A., Waas, A.M.: Multiscale static analysis of notched and unnotched laminates using the generalized method of cells. J. Compos. Mater. **51**(10), 1433–1454 (2017). https://doi.org/10.1177/0021998316651708